Efficient two-layer non-hydrostatic wave model with accurate dispersive behaviour

de Ridder, Menno P.; Smit, Pieter B.; van Dongeren, Ap R.; McCall, Robert T.; Nederhoff, Kees; Reniers, Ad J.H.M.

DOI
10.1016/j.coastaleng.2020.103808

Publication date
2021

Document Version
Final published version

Published in
Coastal Engineering

Citation (APA)
de Ridder, M. P., Smit, P. B., van Dongeren, A. R., McCall, R. T., Nederhoff, K., & Reniers, A. J. H. M. (2021). Efficient two-layer non-hydrostatic wave model with accurate dispersive behaviour. *Coastal Engineering*, *164*, Article 103808. https://doi.org/10.1016/j.coastaleng.2020.103808

Coastal Engineering 164 (2021) 103808

Contents lists available at ScienceDirect

Coastal Engineering

journal homepage: http://www.elsevier.com/locate/coastaleng

Efficient two-layer non-hydrostatic wave model with accurate dispersive behaviour

Menno P. de Ridder [a,*], Pieter B. Smit [e], Ap R. van Dongeren [a,c], Robert T. McCall [a], Kees Nederhoff [b], Ad J.H.M. Reniers [d]

[a] Deltares, Delft, the Netherlands
[b] Deltares USA., Silver Spring, MD, USA
[c] Department of Water Science and Engineering, IHE Delft, the Netherlands
[d] Delft University of Technology, Delft, the Netherlands
[e] Sofar Ocean Technologies, San Francisco, CA, USA

ARTICLE INFO

Keywords:
Dispersive behaviour
Non-hydrostatic model
Wave modelling
XBeach

ABSTRACT

A 2-layer non-hydrostatic model with improved dispersive behaviour is presented. Due to the assumption of a constant non-hydrostatic pressure distribution in the lower layer, the dispersive behaviour is improved without much additional computational time. A comparison with linear wave theory showed that this 2-layer model gives a better result for the dispersion relation and shoaling of waves in intermediate water. This means that the 2-layer model is applicable in shallow and intermediate water depths (up to relative depths *kh* equals 4), whereas the 1-layer model is only applicable in shallow water depths (*kh* smaller than 1). Three laboratory experiments, including a fringing reef and a barred beach, were used to validate the presented mode for different hydrodynamic conditions. Based on these results, it can be concluded that the 2-layer model can be applied to accurately simulate the bulk wave height and spectral properties. The low frequency wave height, the setup and in particular the second order statistics contain more scatter, but the model accurately captured the general trend. Furthermore, the model showed good results for complex bathymetries in shallow to intermediate water.

1. Introduction

Numerical wave models are routinely used to transform offshore waves to nearshore conditions in order to design and evaluate coastal structures, sea defences and port operations (McComb et al., 2009; Cavaleri et al., 2007; Thomas and Dwarakish, 2015). This transformation is efficiently performed by spectral-domain models such as SWAN (Booij et al., 1996), which transform phase-averaged properties of the wavefield, under the assumption of weakly-nonlinear (small wave steepness), homogeneous (small spatial gradients) wave motion. However, as the depth decreases wave steepen and ultimately break, and energy transfers occur that significantly amplify energy levels in the spectral tail and in the infra-gravity band (Elgar and Guza, 1985; Longuet-Higgins and Stewart, 1962; Herbers et al., 1995). Accounting for shallow-water energy transfers in these models is theoretically non-trivial (Agnon et al., 1993; Herbers and Burton, 1997; Janssen and Herbers, 2009), and computationally expensive. As a consequence only approximations are available in practice (Eldeberky, 1997; Salmon et al., 2016). Further, other shallow-water processes such as wave run-up, reflection, and diffraction are typically not accounted for.

Shallow-water wave-driven hydrodynamics are an important driver for morphological change, and to predict e.g. storm impact and coastal flooding a comprehensive description of wave dynamics is needed. Given that typical storm impact modelling time- and spatial-scales are often large compared to the wave motion (O(100–1000) wave periods, O (10) wave lengths), computational restrictions often prevent application of numerical models based on primitive equations (e.g. VOF models). It was shown by Jacobsen and Fredsoe (2014) that VOF models can be applied to model the coastal morphology, but it still requires a significant amount of computational time. That said, increased computational resources have allowed for more accurate descriptions of the hydrodynamics than phase-averaged wave energy models. For example, hydrodynamics are now routinely computed on the wave-group (or infra-gravity) scale through application of the surf-beat model, for example using the XBeach model (Roelvink et al., 2009, 2017) and Delft3D (Reniers et al., 2004; Van Dongeren et al., 2007). XBeach is an

* Corresponding author.
E-mail address: menno.deridder@deltares.nl (M.P. de Ridder).

https://doi.org/10.1016/j.coastaleng.2020.103808
Received 22 June 2019; Received in revised form 21 October 2020; Accepted 23 October 2020
Available online 5 November 2020

open-source model which is applicable for modeling near-shore hydrodynamics, sediment transport and morphodynamics. It has been initially developed for hurricane impacts on sandy beaches in the United States (McCall et al., 2010), but has been further developed for sandy beaches in Europe (Ferreira et al., 2009), coral reefs (Quataert et al., 2015; Pearson et al., 2017) and wave-vegetation interaction (Van Rooijen et al., 2016).

While successful, further improving predictions of wave impact, e.g. effectively predict runup and overwash on reflective beaches (McCall et al., 2014, where short waves dominate), or accurately predicting nonlinear energy transfers, will require phase-resolved hydrodynamics in the nonlinear shoaling region and surfzone. However, to be useful in practice, the phase-resolved approximations need to be as efficient as possible. Invariably, this sets up a trade-off between accuracy and efficiency, which for time-domain models applicable to the surf zone typically puts restrictions on the maximum relative depth kh (k the wavenumber, and h depth) that can be approximated. As kh increases, vertical accelerations (or wave dispersion) can no longer be neglected, and using the (non-dispersive) shallow-water equations to calculate the hydrodynamics becomes inaccurate.

Boussinesq models approximate the effect of vertical accelerations (and vertical structure) of the flow (i.e. dispersion) through inclusion of additional terms in the horizontal momentum and continuity equations (Madsen et al., 1997; Sorensen et al., 1998; Kirby et al., 1998). An overview of the state of the art Boussinesq models and their applications is presented in Brocchini (2013). The governing equations of the Boussinesq models remain effectively 2D in space, at the expense of increased complexity of the governing equations. In their simplest form, these models are restricted to $kh \sim 1$, and to apply these models to deeper water introduces complex higher order terms that are difficult to implement numerically, and can be fundamentally unstable without additional filtering of spurious high frequency modes. In contrast, Non-hydrostatic models explicitly account for vertical accelerations and non-hydrostatic pressure by adopting a 3d description of the flow (Kirby, 2017). Vertical momentum is explicitly solved for, and non-hydrostatic pressure follows by enforcing incompressible flow through a discrete pressure-Poisson type equation (Casulli and Stelling, 1998; Stelling and Zijlema, 2003; Ma et al., 2012). The latter typically dominates the computational effort involved, and can become prohibitive when vertical resolution is fine. These models retain efficiency by adopting a very crude vertical description of the flow. Therefore, several methods were presented to increase the efficiency. Antuono and Brocchini (2013) presented a non-hydrostatic model, which is based on the solution of the Poisson equation for a semi-averaged vertical velocity instead of a dynamic pressure to reduce the computational time. To efficiently resolve a 3D flow field a sub-grid model was presented by Rijnsdorp et al. (2017) in which a limited number of vertical layers are required. However, with a few number of vertical layers the application to wave problems is limited to a finite range of kh values with the single-layer description applicable up to $kh \sim 1$ (Smit et al., 2014; Bai and Cheung, 2013).

To allow for phase-resolved hydrodynamics, XBeach adopted such a single-layer non-hydrostatic approach (Roelvink et al., 2018; Smit et al., 2010), primarily because the single-layer non-hydrostatic framework was compatible with the existing staggered, depth-averaged, shallow--water numerical framework (Stelling and Duinmeijer, 2003). This model has been applied with success (e.g. Pearson et al., 2017; Van Rooijen et al., 2016; McCall, 2015), but practice has shown that the $kh \leq 1$ limit can be restrictive. It may require enforcing the boundary in a region near (or in) the surfzone, where $kh \leq 1$. Here nonlinear contributions can be large and enforcing boundary conditions correctly is difficult since equilibrium solutions based on weakly nonlinear theory no longer apply (Fiedler et al., 2019).

Extending XBeach to allow for multiple layers (similar to Zijlema et al., 2011; Ma et al., 2012) would allow for better dispersive behaviour, but require complete revision of the underlying numerical framework, and come at the cost of substantial decrease in model speed, severely limiting practical space and timescales that can be considered. Further, given all uncertainties in modelling beach response, a full multi-layer implementation is not needed. A modest increase in model applicability would likely provide a sufficiently accurate description of the hydrodynamics.

Here we therefore consider the approach followed in Cui et al. (2014), who proposed an approximate two-layer implementation which effectively describes the pressure using a single control point in the vertical. This approximation is only effective up to $kh \sim$ 3-4 (as opposed to $kh \sim$ 5-6 for a full two-layer description), but the resulting pressure-Poisson equation has the same complexity as the 1-layer model, and consequently the computational burden only increases moderately. Further, formulating the equations in terms of depth-averaged flow, and the velocity difference between the layers, allows for a straightforward inclusion into the existing code-base.

The objective of this paper is to introduce the 2-layer XBeach-nh model and show the accuracy for various conditions. The paper is structured as follows: First the formulation of the 2-layer model is given in section 2. In section 3 the performance of the 2-layer model is shown. A comparison with laboratory experiments is shown in section 4. The results are discussed in section 5 and the conclusions are given in section 6.

2. Model formulation

2.1. Governing equations

We consider the nonlinear shallow water equations including non-hydrostatic pressure (Casulli and Stelling, 1998), formulated on a conventional 3D Cartesian Coordinate system (x, y, horizontal, z vertical positive upwards) with $z = 0$ still water level. Assuming (for brevity) that the flow is uniform in the y direction, the governing equations are

$$\frac{\partial u}{\partial t}+\frac{\partial uu}{\partial x}+\frac{\partial wu}{\partial z}=-\frac{1}{\rho}\frac{\partial (p_{nh}+p_h)}{\partial x}+\frac{\partial \tau}{\partial z} \tag{1}$$

$$\frac{\partial w}{\partial t}+\frac{\partial uw}{\partial x}+\frac{\partial ww}{\partial z}=-\frac{1}{\rho}\frac{\partial q}{\partial z} \tag{2}$$

$$\frac{\partial u}{\partial x}+\frac{\partial w}{\partial z}=0 \tag{3}$$

where t is time, u and w are the horizontal and vertical Eulerian velocities, τ is the shear stress, p_{nh} the non-hydrostatic pressure and p_h the hydrostatic pressure ($p_h = \rho g(\xi - z)$). The water column is vertically bounded by the free-surface elevation (ξ) and the bottom level (d). The free surface elevation is found by integrating the continuity equation over the water depth,

$$\frac{\partial \xi}{\partial t}+\frac{\partial}{\partial x}\int_{-d}^{\xi} u dz=0 \tag{4}$$

The kinematic boundary conditions at the free surface and at the bottom are given by,

$$w=\frac{\partial \xi}{\partial t}+u\frac{\xi}{\partial x} \quad (z=\xi) \tag{5}$$

$$w=-u\frac{\partial d}{\partial x} \quad (z=-d) \tag{6}$$

At the enclosing boundaries, boundary-normal horizontal velocities according to linear wave theory are prescribed. When irregular waves are forced, the wave-wave interactions forcing higher and lower harmonics are also included to minimize the generation of spurious waves (Rijnsdorp et al., 2014; Van Dongeren et al., 2003). Further, weakly reflective boundary conditions are used at the generating boundary to absorb reflected long waves (Smit et al., 2010).

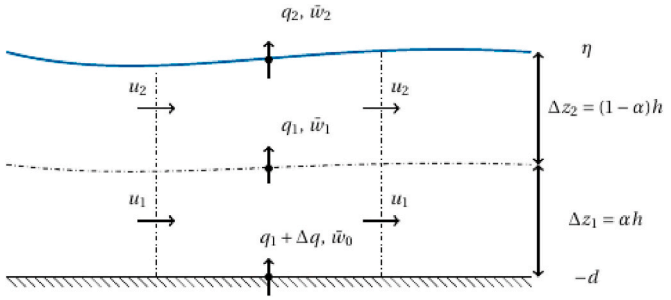

Fig. 1. XBeach-nh 2-layer definitions.

2.2. Two layer approximation

Following Cui et al. (2014) we adopt a 2-layer model of the flow, where the water column is divided into two layers ordered from bottom up, with height $\Delta z_1 = \alpha h$ (bottom layer) and $\Delta z_2 = (1-\alpha)h$. Here α is a layer distribution parameter representing the fraction of the height of the lower layer and the total water depth, h is the water depth ($h = d+\xi$) and the layer interfaces z_j are located at $-d$, $-d+\alpha h$ and ξ (see Fig. 1). Horizontal flow velocities are positioned vertically along the layer center, whereas vertical velocities and the non-hydrostatic pressure are located at the cell face. After integration of the horizontal momentum equation over the vertical, and introducing p_{nh}/ρ as q we find,

$$\frac{\partial \Delta z_j u_j}{\partial t} + g\Delta z_j \frac{\partial \xi}{\partial x} + \frac{\partial \Delta z_j u_j u_j}{\partial x} + \overline{u}_j \omega_j - \overline{u}_{j-1}\omega_{j-1} + \frac{\partial}{\partial x}\left(\Delta z_j \frac{q_j + q_{j-1}}{2}\right) - q_j \frac{\partial z_j}{\partial x} + q_{j-1}\frac{\partial z_{j-i}}{\partial x} - \tau_j + \tau_{j-1} = 0 \tag{7}$$

where the variables with a bar are located at the layer interfaces $\overline{u}_j = u(z_j, x, t)$ and $\omega = \overline{w}_1 - \partial_t z_1 - \overline{u}_1 \partial_x z_1$. Further, the integrated vertical momentum equations in terms of face velocities is given as,

$$\frac{\Delta z_j w_j}{\partial t} + \omega_j \overline{w}_j - \omega_{j-1}\overline{w}_{j-1} + \frac{\partial (\Delta z_j u_j w_j)}{\partial x} + q_j - q_{j-1} = 0 \tag{8}$$

Lastly, the layer integrated continuity equation is given as,

$$\frac{\partial}{\partial x}(\Delta z_j u_j) + \overline{w}_j - \overline{w}_{j-1} - \overline{u}_j \frac{\partial z_j}{\partial x} + \overline{u}_{j-1}\frac{\partial z_{j-1}}{\partial x} = 0 \tag{9}$$

The intended application domain is in relatively shallow water (kd small) and the velocity difference Δu between top and bottom layers is assumed small. To make this assumption explicit we redefine the 2-layer description in terms of depth averaged velocity U and velocity difference Δu ($\Delta u/U \ll 1$) according to,

$$\begin{bmatrix} u_1 \\ u_2 \end{bmatrix} = \begin{bmatrix} 1 & 1-\alpha \\ 1 & -\alpha \end{bmatrix} \begin{bmatrix} U \\ \Delta u \end{bmatrix}; \quad \begin{bmatrix} U \\ \Delta u \end{bmatrix} = \begin{bmatrix} \alpha & 1-\alpha \\ 1 & -1 \end{bmatrix} \begin{bmatrix} u_1 \\ u_2 \end{bmatrix} \tag{10}$$

This is similar to Cui et al. (2014), who considered the difference in momentum between layers ($u_2\Delta z_2 - u_1 \Delta z_1$). Here, the velocity difference is preferred, because it tends to zero in the hydrostatic limit even if the layer distribution are not equidistant. Further, the non-hydrostatic pressure q_0 at the bottom is re-expressed as

$$q_0 = q + \Delta q \tag{11}$$

with $\Delta q = q_1 - q_0$ and where $q = q_1$ denotes the pressure at the center interface. Our objective in the following is to describe the evolution of the two-layer system in terms of the newly introduced variables.

The evolution equation for U may be obtained by summation of equation (7) for $\Delta z_1 u_1$ and $\Delta z_2 u_2$,

$$\frac{\partial (hU)}{\partial t} + gh\frac{\partial \xi}{\partial x} + \frac{\partial}{\partial x}\left(U^2 + \alpha(1-\alpha)(\Delta u)^2 + \frac{h}{2}((1+\alpha)q + \Delta q)\right) - (q+\Delta q)\frac{\partial d}{\partial x} = \tau_0 \tag{12}$$

Further, an evolution equation for Δu follows from subtraction of equation (7) for $\Delta z_2 u_2$ divided by $(1-\alpha)$ from equation (7) for $\Delta z_1 u_1$ divided by α. This results in,

$$\frac{\partial h\Delta u}{\partial t} + \frac{\partial h\Delta u U}{\partial x} + \frac{\omega_1 \overline{u}_1}{\alpha(a-\alpha)} + \frac{\partial}{\partial x}\left(\frac{h}{2}(q+\Delta q)\right) - \frac{q}{1-\alpha}\frac{\partial \xi}{\partial x} - \frac{\Delta q}{\alpha}\frac{\partial d}{\partial x} = -\frac{\tau_0}{\alpha} + \frac{\tau_1}{\alpha(1-\alpha)} \tag{13}$$

where τ_1 is the shear stress between the two layers and τ_0 the bottom shear stress. The shear stress between the layers is related to the differences between the velocities in the layers. Therefore, the closure of the shear stress is formulated in terms of the velocity difference multiplied with an eddy viscosity normalized by the water depth (cf. the Boussinesq closure),

$$\tau_1 = -2\nu\Delta u/h \tag{14}$$

where ν is an eddy viscosity. Note that the internal stress is not meant as an accurate description of turbulent stresses, but added to suppress potential spurious steady-state solutions. The bottom shear stress is given by a quadratic friction law,

$$\tau_b = C_f \frac{U|U|}{h} \tag{15}$$

where C_f is a friction coefficient. For the two vertical momentum equations substitution of U, Δu, q and Δq yields the equations

$$\frac{\partial h w_1}{\partial t} + \frac{\omega \overline{w}_1}{\alpha} + \frac{\partial}{\partial x}(huw_1 + (1-\alpha)h\Delta u w_1) - \frac{\Delta q}{\alpha} = 0. \tag{16}$$

and

$$\frac{\partial h w_2}{\partial t} - \frac{\omega_1 \overline{w}_1}{(1-\alpha)} + \frac{\partial}{\partial x}(hUw_2 - \alpha h \Delta u w_2) - \frac{q}{(1-\alpha)} = 0. \tag{17}$$

Lastly, the two continuity equations can also be expressed in terms of these variables alone. First, addition of two times the kinematic condition at the bottom, $\overline{w}_0 + \overline{u}_0 \partial_x d = 0$, to equation (9) for $j = 1$ yields

$$\frac{\partial}{\partial x}(hU + (1-\alpha)h\Delta u) + \frac{2w_1}{\alpha} - \frac{\overline{u}_1}{\alpha}\frac{\partial z_1}{\partial x} + \frac{\overline{u}_0}{\alpha}\frac{\partial d}{\partial x} = 0 \tag{18}$$

where $\overline{u}_0$ is approximated by $\overline{u}_0 = U + (1-\alpha)\Delta u$. Secondly, addition of twice of equation (9) for $j = 1$ to the equation for $j = 2$ gives

$$\frac{\partial}{\partial x}((1+\alpha)hU + (1-\alpha)\alpha h\Delta u) + 2w_2 - \overline{u}_2\frac{\partial \zeta}{\partial x} - \overline{u}_1\frac{\partial z_1}{\partial x} = 0 \tag{19}$$

Note that, apart from the approximate vertical integration and closure of the shear stresses, no further approximations have been made thus far, and the system expressed in terms of U, Δu, q and Δq is a consistent two-layer approximation of the full equations.

2.3. The reduced two layer system

To simplify the system further, we will assume that $\Delta q/q \ll 1$ so that terms which depend on $q + \Delta q$ can be approximated by q alone and that $\overline{w}_1 = O(\Delta u)$. This assumption limits the application of the model to nearshore shallow water. Due to the approximation of the pressure distribution with a piecewise linear function, the dispersive behaviour of the model is related to the layer distribution. This means that the dispersive behaviour is only accurately described for a limited number of wave frequencies. In relatively shallow water (kh is small) this does not result in a large deviation, because most of the energy is present at

frequencies with an accurately dispersive behaviour. However, in deeper water this assumption leads to an incorrect dispersive behaviour of the dominant waves. Compared to a fully 2-layer model, this assumption results in a larger error in the dispersion relation, but the dispersive behaviour is better than a 1-layer model. Under these assumptions, the evolution of U, Δu, w_2, ζ and q is completely determined by the set of equations consisting of the two horizontal momentum equations

$$\frac{\partial hU}{\partial t}+gh\frac{\partial \zeta}{\partial x}+\frac{\partial}{\partial x}\left(hU^2\right)+\frac{1+\alpha}{2}\frac{\partial hq}{\partial x}-q\frac{\partial d}{\partial x}=0, \tag{20}$$

$$h\frac{\partial \Delta u}{\partial t}+\frac{\partial hU\Delta u}{\partial x}+\frac{1}{2}\frac{\partial hq}{\partial x}+\frac{q}{(1-\alpha)}\frac{\partial \zeta}{\partial x}=-\tau_0-\nu\frac{2\Delta u}{\alpha(1-\alpha)h}, \tag{21}$$

the equation for the mean vertical equation in the top layer,

$$\frac{\partial hw_2}{\partial t}+\frac{\partial hUw_2}{\partial x}-\frac{q}{(1-\alpha)}=0. \tag{22}$$

the continuity equation in the top layer

$$(1+\alpha)\frac{\partial hU}{\partial x}+\left(\alpha-\alpha^2\right)\frac{\partial h\Delta u}{\partial x}+2w_2-\overline{u}_2\frac{\partial \zeta}{\partial x}-\overline{u}_1\frac{\partial z_1}{\partial x}=0 \tag{23}$$

and the global continuity equation

$$\frac{\partial \zeta}{\partial t}+\frac{\partial hU}{\partial x}=0. \tag{24}$$

This set of equations is self-contained, in the sense that neither w_1 nor Δq is required to determine the time evolution of the other variables. This decoupling is achieved by neglecting the coupling to Δq in the horizontal momentum equations, which implies that we assume that the pressure does not change significantly in the lower layer.

Note that, if so required, w_1 can always be obtained from the continuity equation at the bottom. Since the direct coupling between the pressure Δq and the velocities is removed, the pressure Δq acts as a constraint variable that has no dynamical significance for the system as a whole, but merely attains the value necessary to close the balance. If the pressure at the bottom is required, q serves as a good approximation, since if Δq is of significance, that is if $\Delta q/q = O(1)$, the entire procedure becomes invalid, and the full two-layer system has to be used.

To demonstrate the essential components of the reduced pressure 2-layer formulation, we only considered a discrete approach in the vertical, while horizontal components and time are still continuous. The procedure to obtain a fully discrete model is essentially the same as in the Xbeach model and we will only highlight the essential aspect here. Specifically, the equations are discretized with second-order approximations in space and time on a staggered horizontal grid, with pressure, vertical velocities and surface elevation co-located and staggered with respect to horizontal flow. Time integration is explicit, but to solve for the pressure a discrete pressure-Poisson equation has to be solved at each timestep. However, because there is only single unknown pressure point in the vertical, the computational effort involved in constructing and solving the discrete pressure-poisson equation is essentially the same as for a 1-layer model. Hence, compared with a 1-layer model, solving for Δu is the only additional computational effort required.

Lastly, in order to capture breaking of waves with a limited number of vertical layers (1 or 2 in this case), the hydrostatic front approximation is applied (Smit et al., 2013). The procedure reduces the model locally to a shallow water model, using strict momentum conservation to ensure that bulk energy dissipation is represented well. This means that Δu is set to 0, as are the pressures, and the bore capturing properties of the model are identical to the procedure described in Stelling and Duinmeijer (2003), which was verified to work well with the proposed switching mechanism in Smit et al. (2013). A computational cell is set to be hydrostatic when $\frac{\partial \xi}{\partial t} > \alpha_{br} w_{max}$ or when $\frac{\partial \xi}{\partial t} > \beta_{br} w_{max}$ for a cell next to cell where the first condition holds. The cell becomes non-hydrostatic again when $\frac{\partial \xi}{\partial t} < 0$, which represents the passing of the wave crest. It was found that a breaker steepness, α_{br} of 0.4 and a β_{br} of 0.25 gives a good approximation for breaking waves (Roelvink et al., 2017).

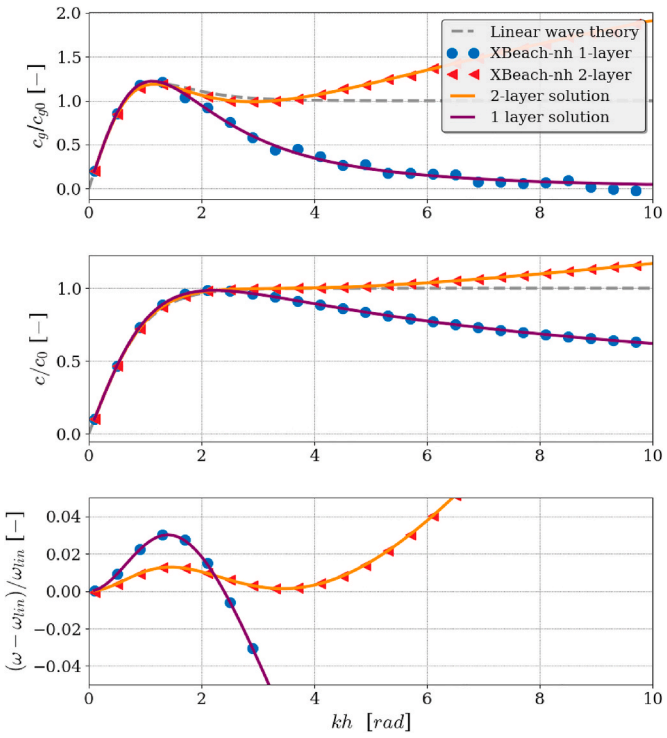

Fig. 2. Dispersive behaviour. Upper panel: group velocity normalized by the deep water group velocity. Middle panel: wave celerity normalized by the deep water celerity. Lower panel: relative error compared to the solution of linear wave theory for the radial frequency (ω). The red triangles are the results obtained with the proposed 2-layer model and the blue circles are results of the 1-layer model. The solution for the numerical dispersion relation (eq. (25)) with an α of 0 and 0.33 is shown as orange and purple lines. (For interpretation of the references to colour in this figure legend, the reader is referred to the Web version of this article.)

3. Validation with analytical solutions

We assess the dispersive behaviour of the proposed model in comparison with the linear wave theory solution and the 2-layer linear solution. Neglecting the non-linear terms and linearizing the equation of the 2-layer model, the dispersion relation of this system can be obtained as (Cui et al., 2014),

$$\omega = k\sqrt{gh\frac{4+(\alpha-2\alpha^2+\alpha^3)(kh)^2}{4+(1+2\alpha-3\alpha^2)(kh)^2}} \tag{25}$$

The accuracy of the dispersion relation for the 2-layer model depends on the layer thickness distribution α. Theoretical, it is possible to select an α, which gives the correct dispersive behaviour for a certain water depth. However, in most applications irregular waves are modelled and an optimum value should be used. Given the numerical dispersion relation (equation (25)), it was found that the relative error in the radial frequency compared to linear wave theory ($(\omega - \omega_{lin})/\omega_{lin}$) is smaller than 0.015 for a kh range from 0 until 5 when α is 0.33. Thus, a layer distribution of 0.33 is used for all the simulations.

3.1. Linear dispersive behaviour

3.1.1. Method

To verify the dispersive behaviour, a linear standing wave in a closed

basin was modelled. By varying the basin length (L), the dispersive behaviour can be shown for different relative water depths (kh). A cosine was set as initial water level with a wave length of $L/2$. The computational grid was discretized with 100 grid points and a simulation time of fifty theoretical wave periods is applied. The water depth was kept constant at 2 m and the amplitude of the initial condition was set to 0.001 m . This means that linear wave theory is valid ($a/L < 0.001$ and $a/d < 0.001$) and that the results can be compared to the linear dispersion relation,

$$\omega = \sqrt{gk \tanh kh} \tag{26}$$

The radial frequency was determined based on zero-crossing analyse. The wave celerity was computed according to $c = k/\omega$ and the group velocity was estimated as $c_g = \Delta\omega/\Delta k$.

3.1.2. Results

The dispersion characteristics of the group velocity, wave celerity and the radial frequency are valid up to a kh of 5 for the 2-layer model, whereas the 1-layer model is valid until $kh = 1$. This is reflected in the relative error of the radial frequency (see Fig. 2). Moreover, the results of both models are equal to the analytical solutions of the numerical dispersion relation (equation (25) with $\alpha = 0$ and $\alpha = 0.33$), which implies that the numerical implementation does not affect the results. Furthermore, there is a different behaviour in deep water for the two models. The 1-layer model underestimates the radial frequency in deep water ($kh > 1$), whereas the 2-layer model the radial frequency is overestimated. As a consequence, the deep water waves travel faster in the 2-layer model than in the 1-layer model (middle panel Fig. 2).

3.2. Linear shoaling

3.2.1. Method

When waves are propagating over a slowly changing bed level, the wave amplitude will shoal due to the conservation of the energy flux which is given by,

$$\frac{\partial P}{\partial x} = \frac{\partial (c_g E)}{\partial x} = 0 \tag{27}$$

where P is the energy flux, c_g the group velocity and E the wave energy (neglecting bottom friction and wave-wave interactions). Based on this relation the shoaling coefficient is given by,

$$K_{shoal} = \frac{A_1}{A_0} = \sqrt{\frac{c_{g,0}}{c_{g,1}}} \tag{28}$$

where A_i is the wave amplitude at location i. Due to the error in the dispersion relation, the shoaling coefficient will deviate from linear wave theory for an increasing kh. To verify this behaviour random waves from a JONSWAP spectrum ($T_p = 8s$ and $H_{m0} = 0.001$m) were modelled over a sloping bathymetry to show the effects of the dispersive behaviour on the shape of the spectrum. It is assumed that a comparison with linear wave theory is possible for these small amplitude waves and that nonlinear affects are negligible.

The waves were forced at a depth of 30 m and after a flat region ($x = 100$ m) the water depth decreases with a slope of 1:30 m till a depth of 2 m. The shoaling coefficient is computed for several output points on this slope based on the ratio of the spectral wave height over the offshore spectral wave height, where the spectral wave height is given as $H_{m0} = 4\sqrt{\int E(f)df}$). To derive the theoretical shoaling coefficient, each wave component from the JONSWAP spectrum is shoaled based on the linear dispersion relation given by Equation (28). This method is also applied to the numerical solution of the dispersion relation to derive the numerical solution of the 1- and 2-layer model. Because the wave height is computed for each wave component, it is also possible to show the shoaling behaviour within the spectrum. A 1:200 sloping beach profile is used to dissipate all the waves. The bottom friction and viscosity are set to zero to neglect wave damping outside the breaking the zone.

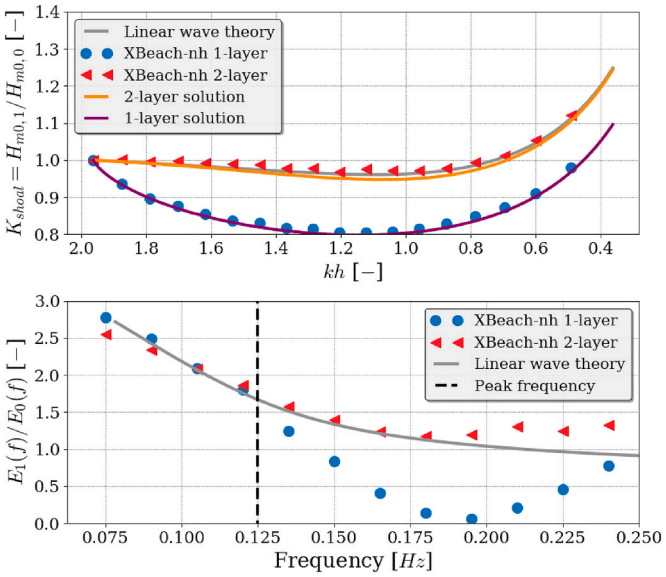

Fig. 3. Shoaling behaviour. Upper panel: results for the shoaling coefficients for different relative depths. Lower panel: ratio deep water ($h = 30m$) energy over shallow water ($h = 2m$) energy for every frequency in the spectrum. The red triangles are the results of the proposed 2-layer model and the blue circles are the results of the 1-layer model. The solution for the numerical dispersion relation (eq. (25)) with an α of 0.33 and 0.0 is shown as orange and purple lines. The method to compute the linear, 1-layer and 2-layer solution of the shoaling coefficient are described in section 3.2.1. (For interpretation of the references to colour in this figure legend, the reader is referred to the Web version of this article.)

3.2.2. Results

The 2-layer model gives an accurate result for the shoaling of waves. The shoaling coefficient is close to zero till a kh of 0.8 from where the waves start to shoal. This result is similar to the solution of linear wave theory (see Fig. 3). The 1-layer model shows a different result, where the energy of the waves decreases over the slope and the modelled wave height is underestimated. The wave height decreases with *20%*, whereas linear wave theory does not show a decrease of wave energy. The numerical results are consistent with their respective analytical dispersion solutions (eq. (25)) for $\alpha = 0.33$ (2-layer) and $\alpha = 0$ (1-layer). This suggest that the numerical implementation is correct. The underestimation of the 1-layer model is mainly caused by the wrong shoaling behaviour of the shorter waves (see Fig. 3 lower panel). The energy in the tail of the spectrum is much lower than predicted with the 2-layer model and the linear wave theory solution.

4. Validation using laboratory data

Three laboratory experiments were modelled with the proposed model to show the performance for different hydrodynamic conditions. First, the energy transfer from a bichromatic wave group to the bound waves over a plane beach is verified. The other two experiments show the accuracy of the wave hydrodynamics of irregular waves over a barred beach and a fringing reef. Both experiments were used as validation, because the hydrodynamics are completely different for both cases.

Each experiment is simulated with the proposed 2-layer model with a layer distribution of 0.0 (1-layer) and 0.33 (2-layer). As the main objective of this paper is to show the validation of the 2-layer model, only the results of the 2-layer model are discussed in this section. The differences between the 1-layer model and 2-layer model are described

in the discussion. All runs were simulated with the default parameters, which is a breaker steepness of 0.4 and a Manning friction coefficient of $0.01 s/m^{1/3}$ (smooth bottoms). The relative bias (rel. bias) and scatter index (SCI) are used to compare the model results with the data of the laboratory experiments. These statistical measures are given by,

$$\text{Rel. bias} = \frac{\sum_{i=1}^{N}\left(x_i - \widehat{x}_i\right)}{\sum_{i=1}^{N}\widehat{x}_i} \tag{29}$$

$$\text{SCI} = \frac{\sqrt{\sum_{i=1}^{N}\left(x_i - \widehat{x}_i\right)}}{\frac{1}{N}\sum_{i=1}^{N}\left|\widehat{x}_i\right|} \tag{30}$$

where x_i is the model output and $\widehat{x}_i$ the measured data.

4.1. Bichromatic waves over a plane beach

4.1.1. Method

In the bichromatic case, a system of two primary waves was forced in a 40 m long flume with a 1/35 sloping beach (Van Dongeren et al., 2007).

The two primary waves will interact and force among other components a bound wave with a difference frequency (sub-harmonic) and a bound wave at the sum frequency (super-harmonic). On a flat bottom and for small amplitude over depth ratios, these second order bound waves are given by,

$$\eta_3 = D(\omega_1, \omega_2, h) a_1 a_2 \cos\omega_3 t - \varphi_3 \tag{31}$$

where a_1 and a_2 are the amplitudes of the primary waves, $D(\omega_1, \omega_2, h)$ is the interaction coefficient derived by Hasselmann (1962), ω_3 is the bound radial frequency and φ_3 is the bound phase. Depending on the profile, the sub-harmonic is dissipated or reflected at the shoreline (Battjes et al., 2004). Therefore, both a test with a reflective sub-harmonic (test A1) and dissipative sub-harmonic (test A4) were modelled. Additionally, test B4 is modelled because it contains the largest amplitude of the bound long wave. The wave conditions of these three tests are shown in Table 1.

During the experiment the waves were generated with a piston-type of wave board with reflection compensation including second order waves. The water level was measured at 80 locations along the flume with a sampling rate of 25 Hz (Fig. 4). In the simulations, the model boundary is located at the first wave gauge (x = 6 m), in order to compare the forced waves with the measurements. To mimic the laboratory environment, the reflection compensation option is applied, and the second order waves were included in the boundary signal. Both the sum interaction ($\omega_1 + \omega_2$), self interactions($\omega_i + \omega_i$) and the difference interactions ($\omega_1 - \omega_2$) were included at the boundary signal based on equation (31) to minimize spurious waves (Madsen and Sørensen, 1993). A resolution of 0.025 m was used to discretise the domain, which corresponds to 30 grid points per wave length for the super-harmonics.

Table 1
Wave conditions of the three experiments which are modelled. f_1 and f_2 are the primary wave frequency, f_b is the bound sub-harmonic frequency and kd the maximum normalized water depth.

Test	f_1 [Hz]	f_2 [Hz]	f_b [Hz]	a_1 [m]	a_2 [m]	kd [rad]
A1	0.67	0.48	0.19	0.06	0.012	2.0
A4	0.62	0.53	0.09	0.06	0.012	1.8
B4	0.65	0.50	0.15	0.06	0.036	1.94

The threshold water depth above which cells are considered wet, was changed to 0.001 m correctly reproduce the reflection of the long waves.

The validation is based on the total wave energy and the energy of the super and sub-harmonic respectively. The total wave height is computed from the spectral moment as $H_{total} = 2\sqrt{2m_0}$ where m_0 is given by $m_0 = \int E(f)df$. The sub-harmonic wave height (H_{sub}) is obtained by applying a band filter to the difference frequency including their higher components ($m\Delta f = m(f_1 - f_2)$ up to the Nyquist frequency. In this way the steepening of the sub-harmonics is also included in the signal. In a similar way the wave height of the super-harmonic was determined (H_{super}).

4.1.2. Results

The wave transformation of the primary waves and the accompanying sub-harmonic is modelled accurately with 2-layer model for the three tests (see Table 2). Only the cross-shore distribution of the wave heights is shown for experiment A1 and A4 because the long wave behaviour of experiment A1 and B4 are very similar. In all tests, the energy of the bichromatic wave group is almost constant until the breakpoint, after which the wave height decreases (see Fig. 5 panel A). Only in test B4 breaking initiated slightly further offshore ($\approx 1m$). This small offset in test B4 could be caused by a different breaking mechanism due to the larger wave heights, which require a larger breaking steepness.

Due to the slowly decreasing water depth, the energy of the sub-

Table 2
Statistics for tests A1, A4 and B4 of the bichromatic wave group experiment for the proposed and current version of the model with default settings. The total statistical measures were computed for all the observation points for each individual test (A1, A4 and B4).

Run	H_{total}		H_{sub}		H_{super}	
XBeach-nh 2-layer	SCI	Rel. bias	SCI	Rel. bias	SCI	Rel. bias
A1	0.06	−0.013	0.13	0.015	0.17	0.050
A4	0.04	−0.002	0.14	−0.012	0.2	0.056
B4	0.04	0.033	0.10	0.106	0.21	−0.009
total	0.04	0.033	0.22	0.150	0.21	−0.009
XBeach-nh 1-layer						
A1	0.07	−0.037	0.14	−0.006	0.18	0.015
A4	0.05	−0.022	0.19	−0.015	0.19	0.022
B4	0.06	0.030	0.17	0.104	0.22	−0.036
total	0.06	0.030	0.21	0.140	0.22	0.036

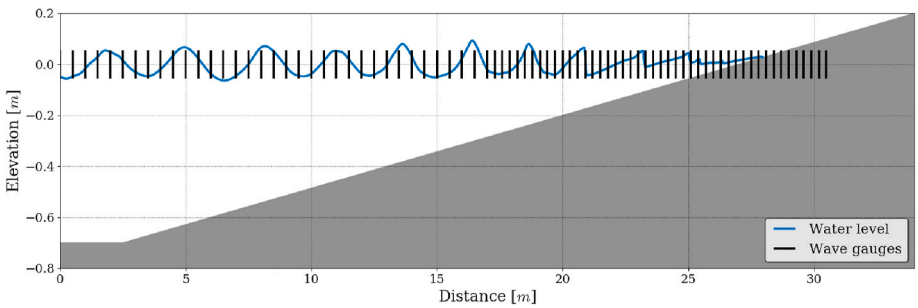

Fig. 4. Laboratory set-up of the bichromatic wave experiment. The vertical lines represent the wave gauges (Van Dongeren et al., 2007).

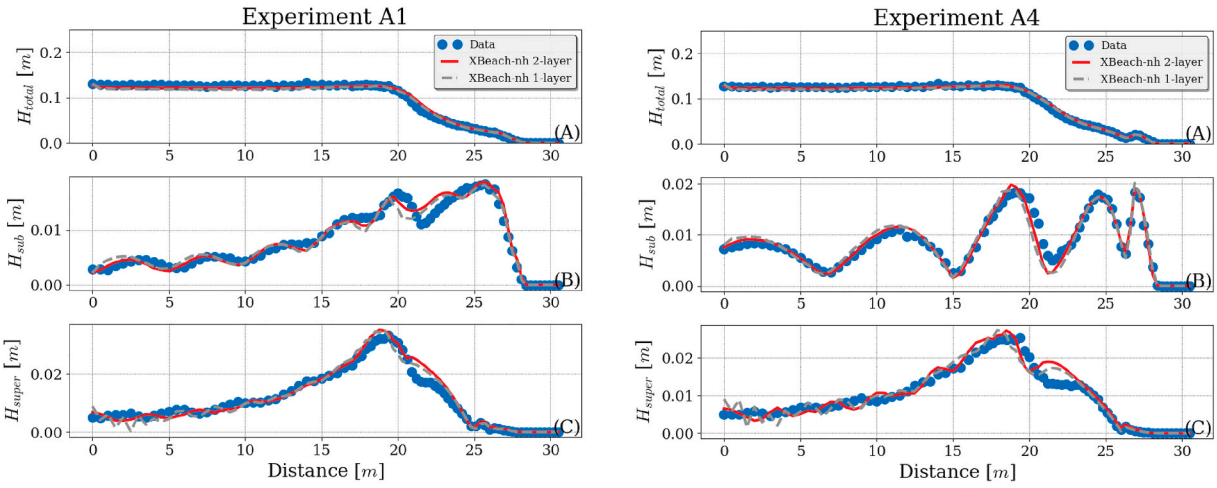

Fig. 5. The transformation of the total wave height H_{total} for tests A1 and A4 (panel A), the low-passed sub-harmonic wave height H_{sub} (panels B) and the high-passed super-harmonic wave height H_{super} (panel C).

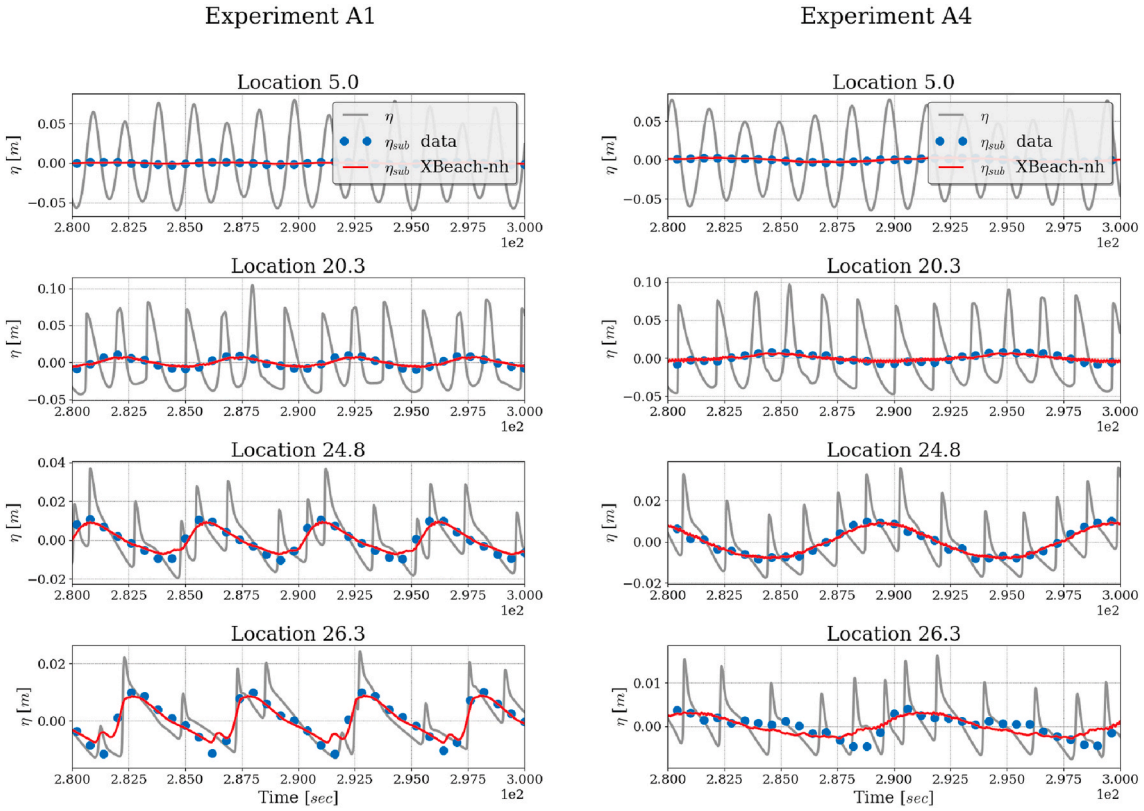

Fig. 6. Time series at locations in the flume of experiment A1 and A4. The total measured water level elevation (grey solid line), the low-passed observed sub-harmonic (blue dots), and the low-passed modelled sub-harmonic (red line). (For interpretation of the references to colour in this figure legend, the reader is referred to the Web version of this article.)

harmonic wave shoals until the initiation of breaking (see Fig. 5 panel B). However, the behaviour of the sub-harmonic between the tests is different. In the case of test A1 and B4 most of the sub-harmonic energy is dissipated, whereas a standing wave pattern is visible for test A4 due to reflection. This behaviour is captured with the numerical simulations, which shows that the 2-layer model is capable in modelling the energy transfer to the sub-harmonic and capturing the dissipation and reflection of the sub-harmonic at the shoreline (see Fig. 5 panel B).

In all three tests a similar behaviour of the super-harmonic is found. The super-harmonic energy increases with a decreasing water depth until the breakpoint, where the super-harmonic is dissipated. This behaviour is also found in the numerical simulation, but the oscillation in the shoaling region is slightly different in the numerical simulations. This oscillation is caused by free spurious waves which arise due to the mismatch at the boundary. A simulation without super-harmonics in the boundary conditions showed a similar oscillation with a larger amplitude, which indicates that these oscillations are caused by a superposition of free and bound super-harmonics. Due to the deviation in the dispersive behaviour of the free waves, the wave length is slightly different than the measured oscillation.

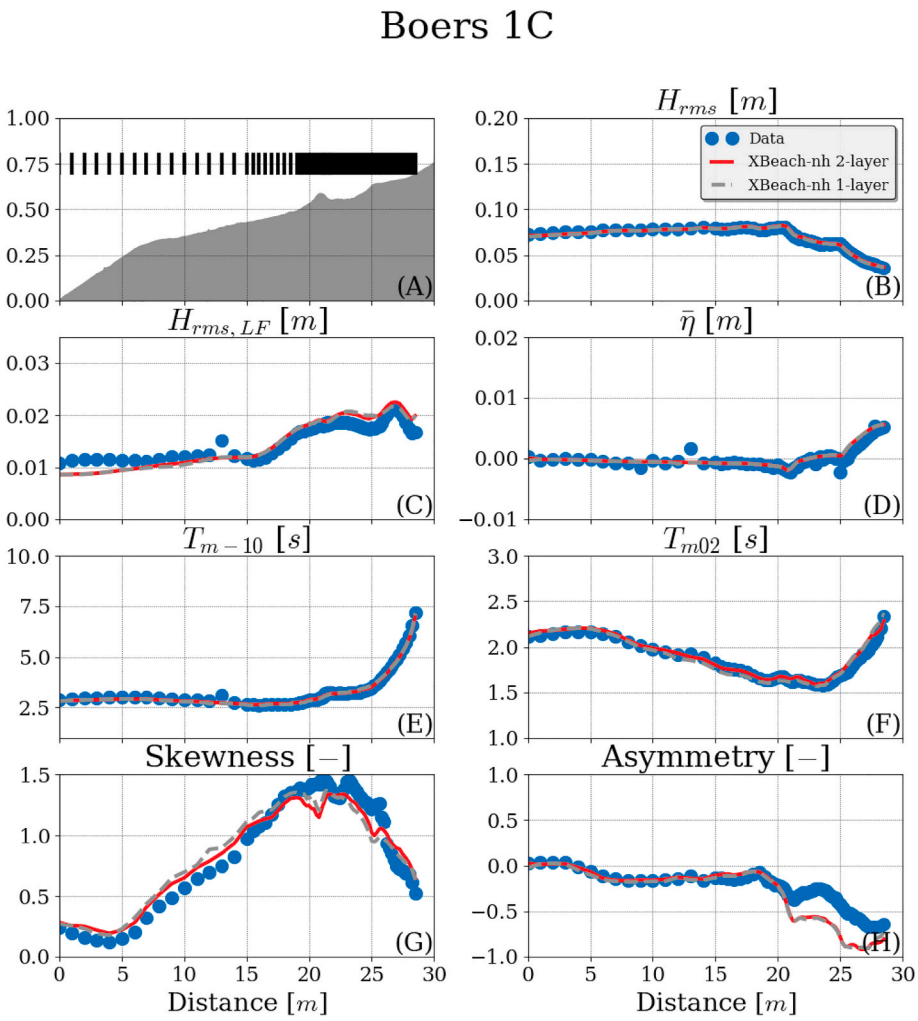

Fig. 7. Validation of the proposed model against Boers test 1C. The red line is the result computed with the proposed model, the grey line those obtained with the current 1-layer model, and the observations are shown with blue dots. The comparison is made for the total wave height (panel B), the LF-wave height (panel C), the setup (panel D), the spectral wave period (panel E), zero-crossing period (panel F), the skewness (panel G) and the asymmetry (panel H). In panel A the bed level and the instantaneous surface elevation is shown. (For interpretation of the references to colour in this figure legend, the reader is referred to the Web version of this article.)

Because long waves are important for numerous coastal applications (e.g. coastal erosion or resonance), we also verified the sub-harmonic wave shape. The time series of the primary and sub-harmonic show that the 2-layer model is capable of accurately simulating the shape of the sub-harmonic (see Fig. 6). The dissipation of the sub-harmonic for test A1 is clearly visible. The wave shape becomes more asymmetrical closer to the shoreline. When the wave shape becomes too asymmetrical the sub-harmonic starts to dissipate and from that point the amplitude reduces. This behaviour is not found for the reflective sub-harmonic, where the wave shape is almost constant for the different locations. In this case the amplitude differs between the different time series due to a standing wave pattern. There is a small deviation for test A4 close to the shoreline, but in general the steepness of the sub-harmonic is accurately modelled. This means that not only the energy transfer to the sub-harmonic is reproduced, but that also the energy transfer to the higher components of the sub-harmonic is captured.

4.2. Irregular waves over a barred beach

4.2.1. Method

For the case of irregular waves over a barred beach, three experiments observed by Boers (1997) were modelled. In this laboratory flume case, a concrete beach profile with an offshore depth of 0.75 m and a bar at 25 m (see Fig. 7 panel A) was constructed. Random waves were generated at the wave maker for three different wave steepnesses based on a JONSWAP spectrum. The wave conditions of the three tests are shown in Table 3. The surface elevation was measured at 70 locations with a spatial resolution of 0.1 m in the surf-zone and 1 m in the shoaling zone.

Table 3
Wave conditions for the tests 1A, 2B and 1C of the Boers experiments. The f_p is the peak period, H_s the significant wave height, kh the relative depth of the peak period and kA the relative steepness of the peak period given the significant wave height.

Test	T_p [s]	H_s [Hz]	kh [rad]	kA [rad]
1A	2.1	0.16	0.93	0.20
1B	2.1	0.22	0.93	0.27
1C	3.4	0.1	0.53	0.07

The numerical model is discretized with a grid resolution of 0.02 m which corresponds to at least 20 grid cells for waves at 3 f_p. The boundary is located at the first wave gauge and the model is forced with the measured high-passed (0.15 Hz) water level time series under the assumption that most of the short waves break at the beach. To account for the incoming long waves, the theory of Hasselmann (1962) was used as implemented by Van Dongeren et al. (2003).

The results are verified for the total wave height ($H_{rms} = 2\sqrt{2m_0}$), the low frequency wave height ($H_{rms,LF} = 2\sqrt{2m_0}|_{f<0.15Hz}$), the setup ($\langle\eta\rangle$), the energy period ($T_{m-1,0} = m_{-1}/m_0$), the mean zero-crossing period ($T_{m02} = \sqrt{m_0/m_2}$), skewness and asymmetry. The wave moment, m_n, is given by $\int f^n E(f) df$ where an upper bound of $4f_p$ is used to neglect the noise. The skewness and asymmetry are given by,

Table 4
The statistical measured for the different runs of the Boers experiments. The results are shown for the 1-layer model and the 2-layer model. The total statistical measure was computed for all observation points for each individual test (1A, 1B and 1C).

Run	H_{rms}		$H_{rms,LF}$		$\bar{\eta}$		$T_{m-1.0}$		T_{m02}		skewness		asymmetry	
2-layer	SCI	Rel. bias	SCI	Rel. bias	SCI	Rel. bias	SCI	Rel. bias	SCI	Rel. bias	SCI	Rel. bias	SCI	Rel. bias
1A	0.04	−0.006	0.1	0.06	3.53	0.07	0.07	0.04	0.05	0.01	0.17	−0.13	1.76	1.29
1B	0.06	−0.03	0.08	−0.06	2.49	0.25	0.04	−0.01	0.05	−0.02	0.15	−0.1	1.54	1.32
1C	0.02	0.003	0.09	0.03	7.88	3.92	0.03	−0.02	0.02	0.01	0.12	−0.03	0.72	0.52
total	0.05	−0.018	0.09	0.002	3.48	0.271	0.11	0.03	0.03	0.0	0.14	−0.07	1.17	0.92
1-layer														
1A	0.06	−0.022	0.09	0.04	3.52	−0.11	0.08	0.06	0.07	0.03	0.14	−0.06	1.72	1.22
1B	0.07	−0.03	0.08	−0.05	2.5	0.22	0.12	0.06	0.05	−0.01	0.14	−0.11	1.55	1.26
1C	0.02	−0.006	0.09	0.02	8.28	4.02	0.03	−0.02	0.03	0.0	0.12	−0.02	0.74	0.55
total	0.06	−0.025	0.09	−0.002	3.47	0.187	0.14	0.06	0.05	0.0	0.13	−0.06	1.17	0.90

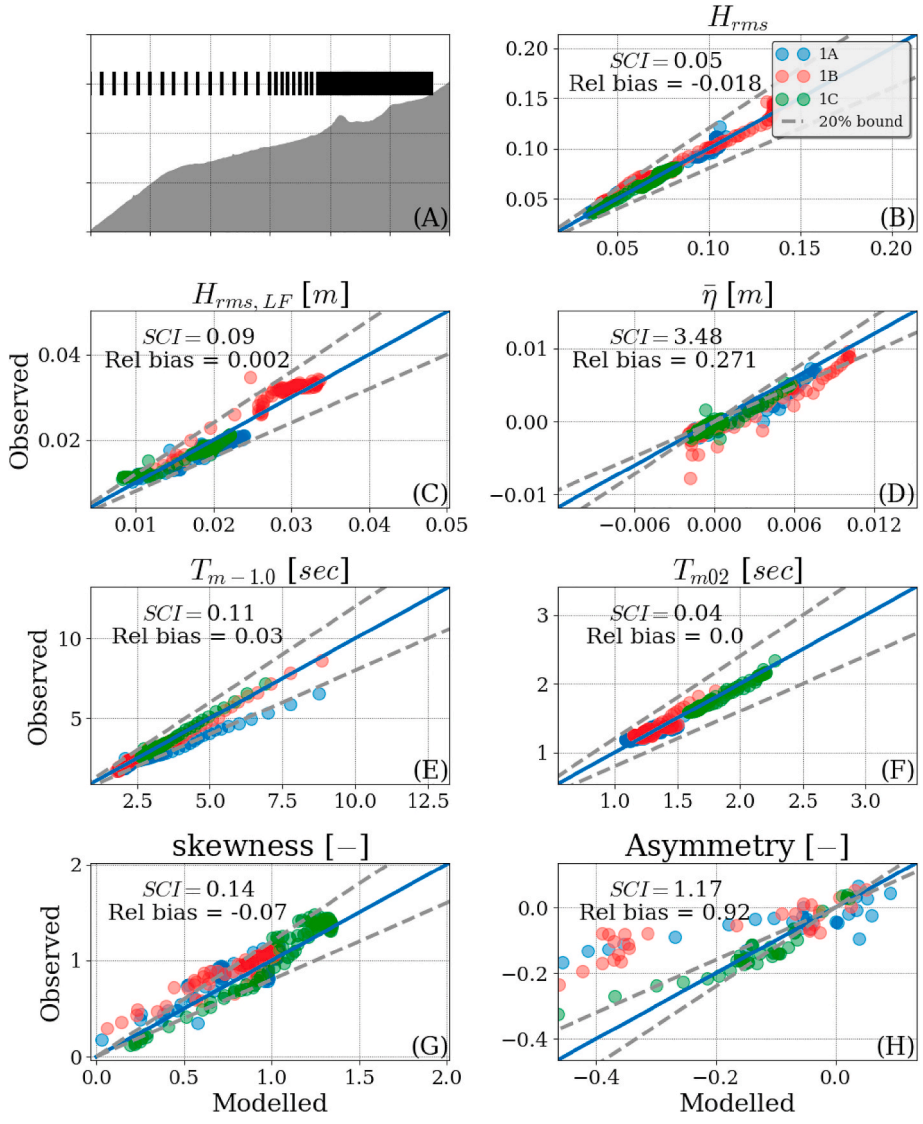

Fig. 8. Scatterplots of computed and observed wave properties for the three Boers experiments. The comparison is made for the total wave height (panel B), the LF-wave height (panel C), the setup (panel D), the spectral wave period (panel E), zero-crossing period (panel F), the skewness (panel G) and the asymmetry (panel H). In panel A the bed level and the instantaneous surface elevation is shown.

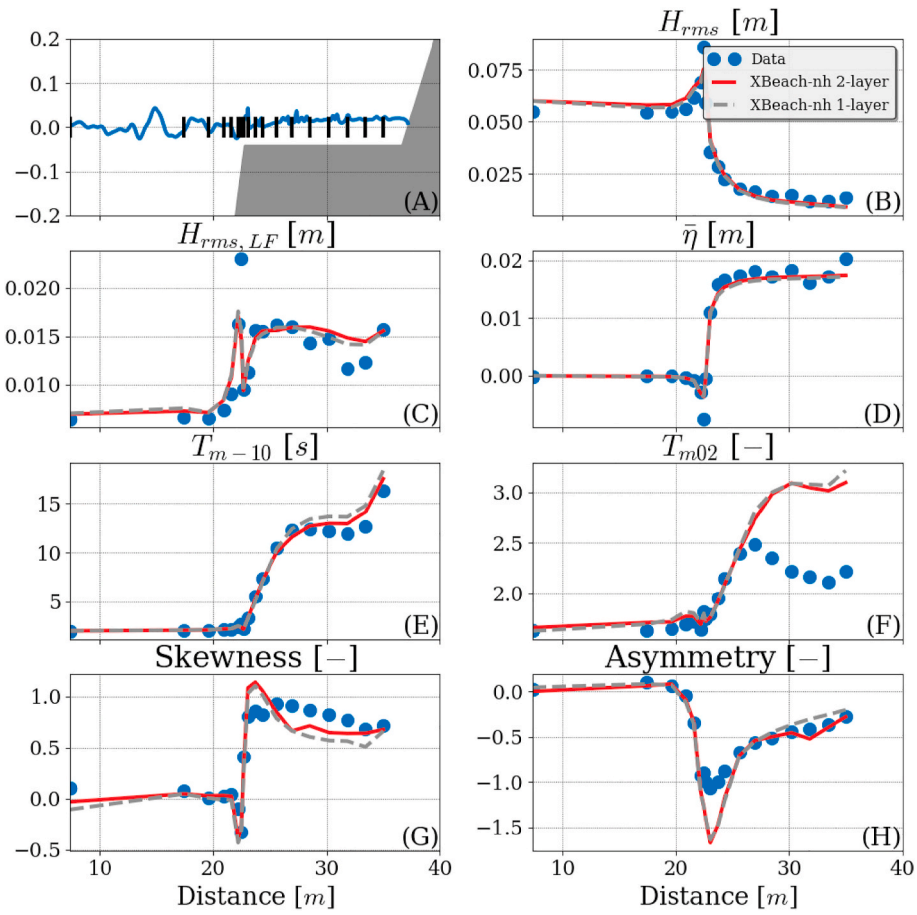

Fig. 9. Validation of the proposed model against Buckley et al. (2015) observations. The red line is the result computed with the proposed model, the grey line those obtained with the current 1-layer model, and the observations are shown with blue dots. The comparison is made for the total wave height (panel B), the LF-wave height (panel C), the setup (panel D), the spectral wave period (panel E), zero-crossing period (panel F), the skewness (panel G) and the asymmetry (panel H). In panel A the bed level and the instantaneous surface elevation is shown. (For interpretation of the references to colour in this figure legend, the reader is referred to the Web version of this article.)

$$Sk = \frac{\langle (\eta - \bar{\eta})^3 \rangle}{\langle (\eta - \bar{\eta})^2 \rangle^{3/2}} \tag{32}$$

$$As = \frac{\langle \mathscr{H}(\eta - \bar{\eta})^3 \rangle}{\langle (\eta - \bar{\eta})^2 \rangle^{3/2}} \tag{33}$$

where η is the wave signal, $\bar{\eta}$ the mean of the signal and $\mathscr{H}$ the Hilbert transform of the water level signal.

4.2.2. Results

The bulk wave statistics and the spectral properties are accurately reproduced for all tests, whereas the second order statistics are reasonable accurate predicted (see Table 4 and Fig. 8). First the hydrodynamic behaviour of the barred beach is shown for test 1C, which shows comparable results as the other tests. The main difference between the three tests is that the waves shoal in test 1C, whereas the waves are already breaking at the wave maker for the two other tests. Secondly, the performance of the 2-layer model is shown for a comparison of the three tests with the measurements.

In test 1C the waves shoal till the bar from where the waves start to break (Fig. 7 B). The short waves force the low frequency waves (LF-waves), which gain energy till the breaker bar. In the breaker-zone, the LF-waves partly reflect and dissipate (Fig. 7 C). Due to the decrease of radiation stresses in the breaker-zone, the water level is elevated resulting in a setup (Fig. 7 D). These bulk wave statistics are well captured with the numerical simulations.

Considering the spectral periods, the 2-layer model shows good results. The results for the T_{m02} and $T_{m-1.0}$ indicate that the spectral shape is well captured, where T_{m02} emphasizes the high-frequency tail of the spectrum and the$T_{m-1.0}$ lower frequency part. The spectral period shows that close to the shoreline most of the energy is present in the long waves (Fig. 7 F). The energy transfer to higher components is visible in the zero-crossing period which becomes smaller towards the bar (Fig. 7 F). From the bar the waves become too nonlinear and start to break, which result in an increase of the zero-crossing period.

The accuracy of the second order statistics is verified by means of the skewness and asymmetry, the trend of which is captured correctly (Fig. 7 G and H). The waves become more skewed closer to the breaking point, which means that the peaks become higher compared to the trough. When the waves start to break the skewness decreases because most of the large waves break. The asymmetry remains almost constant until the bar after which the waves become more pitched forward. Thus, the asymmetry becomes more negative at the bar and at the second breaking point.

When the results of three runs are compared to the data, the three tests give a similar result (see Fig. 8).

The total wave energy is accurately reproduced for all three tests (Fig. 8 B). Considering the LF-wave energy there is more scatter (Fig. 8 C). A reason for the scatter could be that the reflection compensation in the wave flume didn't work properly, because of breaking waves at the wave paddle (Boers, 2005). However, the LF-wave transformation is accurately simulated with the proposed model. Both shoaling before the bar and dissipation from the bar are accurately reproduced. The mean water level shows a similar result as the physical experiments (Fig. 7 D), but for all three experiments the setup in the breaker zone is slightly overestimated. Since the mean of all data points is very close to zero, the statistical scores are relatively larger.

When the spectral periods are compared, the three tests show a similar result. Both the test with the shortest waves (test 1C) and the longer waves show good results (Fig. 8 F). Only for test 1A is there an overestimation of the $T_{m-1.0}$ close to shoreline ($x > 25$ m). This causes

Table 5
Model set-up of the Buckley experiments. The reef depth ($h_{0,r}$) represents the still water depth at the reef and the kh is computed for the peak period.

test	H_{rms} [m]	T_p [s]	$h_{0,r}$ [m]	kh of T_p [rad]
1	0.03	2.26	0.04	0.85
2	0.06	2.26	0.04	0.85
4	0.12	2.26	0.04	0.85
9	0.06	2.26	0.00	0.82
12	0.06	2.26	0.09	0.89

the much higher scatter index of the $T_{m-1.0}$ compared to the T_{m02} (Fig. 8 E). This deviation is caused by too much energy dissipation at the peak frequency, which results in a higher modelled $T_{m-1.0}$ for test 1A.

Most of the scatter is visible in the second order statistics (Fig. 8 G and H). For test 1C the second order statistics are well reproduced, but there is larger discrepancy close to the shoreline for the other two tests. The trend is very similar to the measurements, but the proposed model overestimates the asymmetry close to the shoreline in the case of test 1A and 1B. This deviation is the result of the numerical breaking mechanism. The hydrostatic front approximation is based on the energy dissipation of a bore, where the bore-face can become very steep. In the case of spilling/plunging waves this would result in a more negative wave asymmetry in the model. Since the wave period is larger for test 1B and 1C, more spilling/plunging type of breakers are presented in these tests and, therefore, the deviation in wave asymmetry is larger for these two tests.

4.3. Irregular waves over a fringing reef

4.3.1. Method

The third laboratory validation case is Buckley et al. (2015) of a fringing coral reef. Contrary to the previous mildly-sloping barred beach case, waves break violently on the steep reef face, causing large radiation stress gradients and large wave-induced setup on the reef platform. In addition, long waves are generated in the narrow breaker zone due to the breakpoint mechanism (Symonds et al., 1982).

The Buckley et al. (2015) observations are taken in a 55 m long flume with a wooden fringing reef profile consisting of a 1:5 reef slope, a 14 m long reef flat and a 1:12 sloping beach (see panel A of Fig. 9). In the present analysis, only the runs over a smooth bed were used as validation. From the 16 available tests, five were selected for validation, where both the water level and the wave height was varied (see Table 5).

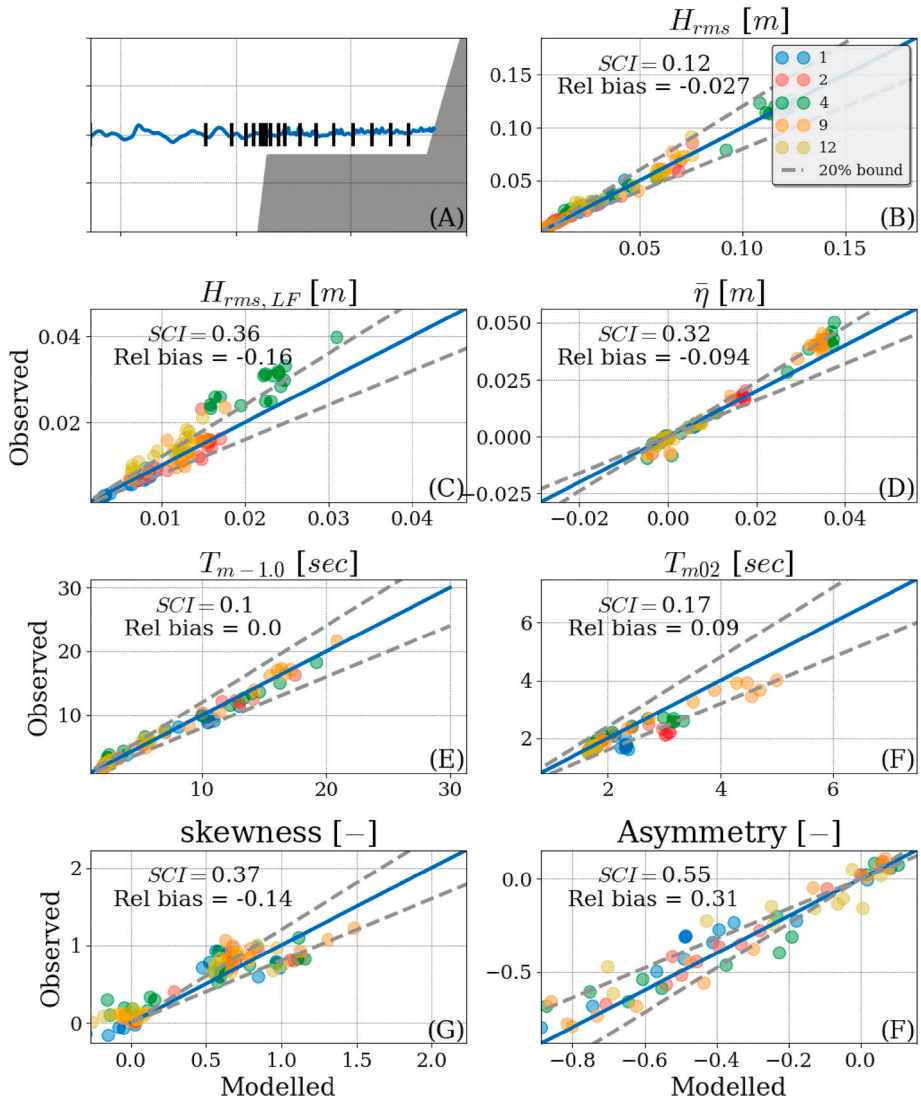

Fig. 10. Scatterplots of computed and observed wave properties for the Buckley experiments for the 2-layer model: total wave height (panel B), the LF-wave height (panel C), setup (panel D), the spectral wave period (panel E), zero-crossing period (panel F), the skewness (panel G) and the asymmetry (panel H). In panel A the bed level and the instantaneous surface elevation is shown.

Table 6
The statistical measures for the different runs of the Buckley experiment with the default settings. The results are shown for the 1-layer model and the 2-layer model. The total statistical measures were computed for all the observation points for each individual test .

Run	H_{rms}		$H_{rms,l\Delta f}$		$\overline{\eta}$		$T_{m-1.0}$		T_{m02}		skewness		asymmetry	
2-layer	SCI	Rel. bias	SCI	Rel. bias	SCI	Rel. bias	SCI	Rel. bias	SCI	Rel. bias	SCI	Rel. bias	SCI	Rel. bias
1	0.11	−0.044	0.11	0.05	0.35	0.25	0.16	0.09	0.18	0.11	0.46	−0.17	0.35	0.24
2	0.12	0.024	0.18	0.02	0.16	−0.03	0.09	0.02	0.23	0.13	0.35	−0.07	0.47	0.28
4	0.1	−0.034	0.37	−0.29	0.27	−0.14	0.1	−0.02	0.14	0.05	0.38	−0.12	0.81	0.46
9	0.11	−0.037	0.17	−0.05	0.25	−0.15	0.05	−0.01	0.17	0.1	0.32	−0.13	0.46	0.26
12	0.12	−0.044	0.24	−0.21	0.41	0.27	0.09	−0.08	0.04	0.03	0.38	−0.2	0.57	0.32
total	0.12	−0.027	0.36	−0.157	0.32	−0.094	0.1	0.01	0.17	0.09	0.37	−0.14	0.55	0.31
1-layer														
1	0.12	−0.06	0.12	0.06	0.32	0.21	0.24	0.13	0.22	0.14	0.46	−0.2	0.32	0.19
2	0.12	0.002	0.16	0.02	0.17	−0.05	0.13	0.06	0.24	0.14	0.4	−0.18	0.47	0.22
4	0.1	−0.043	0.38	−0.3	0.27	−0.14	0.09	−0.05	0.15	0.07	0.37	−0.18	0.81	0.44
9	0.11	−0.045	0.19	−0.08	0.26	−0.16	0.07	−0.02	0.19	0.11	0.42	−0.24	0.45	0.32
12	0.12	−0.037	0.23	−0.21	0.42	0.27	0.12	−0.09	0.06	0.05	0.37	−0.21	0.56	0.35
total	0.12	−0.036	0.37	−0.167	0.33	−0.101	0.13	0.0	0.19	0.10	0.40	−0.20	0.54	0.3

The model is forced with a TMA spectrum analogous to the laboratory experiments. To account for the finite volume of water in the wave-flume, the bed level is corrected within XBeach. Due to the relative large setup on the reef, the water depth at the boundary is slightly shallower than the still water depth in the wave-flume. Thus, this difference at the offshore boundary is added to the bed level in XBeach. Furthermore, a spatially-varying grid was used to optimise the computational effort. The grid resolution is based on 80 grid points per wave length (period of 2 s). The model boundary is located at the first measurement location and the model is forced with random components from a TMA spectrum including second order waves.

4.3.2. Results

The same wave properties as used in the Boers test were validated. The bulk wave properties and spectral properties are well reproduced for all tests and the second order statistics are predicted reasonably accurately (see Fig. 10 and Table 6). The cross-shore distribution of the wave properties for the most representative run (test 2) is shown in Fig. 9. First, the results of test 2 are described to show the behaviour of the hydrodynamic conditions for a fringing reef. Thereafter, the model performance is shown for all the five tests.

At the fore-reef the waves shoal rapidly till the breaking point. The waves break in a narrow breaking zone at the reef crest (Fig. 10 B), from where the wave energy significantly reduces. In this breaking zone the LF-waves are generated, which propagate over the reef flat (Fig. 10 C). The reflection of the LF-waves at the shoreline causes the standing wave pattern in the LF-wave height profile. Due to the absence of most of the short waves, the LF-waves are dominant on the reef flat. At the reef crest there is a spike in the LF-wave energy, which both visible in the numerical results as the measurements. It is not known which processes causes this spike. The breaking waves also result in a water level gradient at the reef crest, which gives rise to a constant setup on the reef flat (Fig. 10 D). The numerical simulations show good agreement for the setup on the reef flat. Before the reef flat, there is a setdown in the shoaling region. This behaviour is also visible in the numerical results, but the model underestimates this setdown.

Based on the spectral wave periods, it can be seen that most of the energy is transferred to the LF-waves on the reef flat (see Fig. 9 E). The $T_{m-1,0}$ increases significantly on the reef flat, which is also visible in the performance of the 2-layer model. The 2-layer model results do not agree with the observations of T_{m02}, the metric describing the high-frequency tail. The observed T_{m02} increases on the reef crest and decreases again on the reef flat. However, the modelled T_{m02} keeps increasing on the reef flat. Since most of the short waves break at the reef crest, most of the energy is present at the lower frequencies. Therefore, the T_{m02} is more sensitive for the lower frequencies than the high-frequency tail at the reef flat. Due to a slight overestimation of the energy at the lower frequencies, the modelled T_{m02} is larger than the measured T_{m02}.

Apart from a transformation of the bulk wave statistics, the second order statistics also transform over the reef. Before the reef crest the skewness and asymmetry are constant due to the horizontal bed level (Fig. 9 E and F). The skewness decreases just before the breaking point and then increases to an almost constant value on the reef flat. The asymmetry increases until the breaking point, where the most pitch-forward wave shape is found. Then the waves start to break, and the asymmetry decreases significantly. Due to the shallow water at the reef flat, the asymmetry becomes less negative on the reef flat. This general behaviour of both the skewness and asymmetry is also visible in the numerical results.

The other tests show a comparable result as test 2. In all tests the total wave height is accurately predicted (see Fig. 10 B). There is more scatter in the LF-wave height (see Fig. 10 C). This is mainly caused by test 4 and 12, where the LF-wave energy is underestimated (see also Table 6). It is not known why these tests give a different result for the LF-wave energy. Apart from this deviation, the LF-wave energy distribution is matching the data for all the tests. Offshore of the reef crest the LF-wave energy is relatively low and increases rapidly at the reef crest. Considering the mean water level, all tests give a good result (see Fig. 10 C). There is only a small underestimation ($\approx 1mm$) of the setup for test 4 and 9 and an overestimation for test 1 and 12 (see Table 6). As the setup is the result of the radiation stress gradients in the breaker zone, it is sensitive to the breaking mechanisms which control the radiation stress gradient. The deep-water surf similarity parameter for tests 4 and 9 ($\zeta = 1.7$ and $\zeta = 2.2$) is lower than for test 1 and 12 ($\zeta = 3.3$ and $\zeta = 2.3$Buckley et al., 2015). Thus, the hydrostatic front approximation results in a slightly smaller radiation stress gradient, causing a lower setup, for a lower surf similarity parameter. Similar to the Boers test, more scatter is present in the skewness and asymmetry (see Fig. 10 E and F). In all tests the proposed model overestimates the asymmetry on the reef crest. This results in the large scatter index and relative bias. Just as in the Boers test, this could be caused by the single-value representation of the surface elevation and the simplified breaking mechanism. It is for example not possible to simulate overturning waves, which could result in too asymmetrical waves in the numerical simulation, whereas in reality the waves would become less steep due to a different breaking mechanism. However, the model is capable in simulating the correct cross-shore profile of these second order statistics for all tests.

5. Discussion

The improved dispersive behaviour of this 2-layer model is desired for multiple applications. The main reason to apply the presented model is when the boundary needs to be in deep water. This could be necessary

Table 7
Wave conditions of the two experiments which are modelled from the Beji and Battjes (1993) experiments.

Test	H_{m0} [m]	T_p [s]	kh of T_p [rad]
JONSWAP Short Non-breaking waves (jsn)	0.041	1	1.7
JONSWAP Long Non-breaking waves (jln)	0.029	2.5	0.53

when the wave data, needed for the boundary conditions, is only present in intermediate water or when the forced wave heights are too large/nonlinear in shallow water. With the 1-layer model this would result in a wrong shoaling behaviour and underestimation of the wave height (Fig. 3), whereas the 2-layer model could be still applicable. Because the laboratory experiments of irregular waves were all performed in shallow water ($kh < 1$ for the peak period), this wrong shoaling behaviour is not very pronounced. Only the short waves in the tail of the spectrum are affected by the error in the dispersion relation, but this error is limited as these short waves do not contain much energy. In the experiments of a bichromatic wave group over a plane beach the relative water depth is close to 2 (indeterminate water). This means that there is a significant error in the dispersion relation for the 1-layer model, but because of the relative simple bathymetry this has no large effect on the results. The primary waves hardly shoal due to the small slope of the bed level, which therefore does not result in an amplitude error.

Apart from the water depth, an improved dispersive behaviour would also give a better result for the energy transfer to the shorter waves, which would mostly affect the T_{m02}, skewness and asymmetry. In general, the results of the 2-layer model are slightly better than the 1-layer model, but this difference is very small (Tables 6 and 4). In appendix Appendix A the error in the resonant mismatch, related to the energy transfer, is shown for the 1-layer and 2-layer model. This result shows that the error in the resonant mismatch is relative small (10%) for the 1-layer model when the $kh < 1$. Thus, the energy transfer to these higher components is still reasonable accurate predicted with the 1-layer model when the kh is small. Thus, the energy transfer to these higher components is still reasonable accurate predicted with the 1-layer model when the kh is small. only in the energy of the super-harmonic in the experiment of a bichromatic wave group a deviation is visible between the two models. The 1-layer model cannot correctly force the super-harmonic at the boundary, which result in a spurious wave near the boundary.

Although these results do not show a clear improvement of the 2-layer model in shallow water, there is another reason to apply the 2-layer model in shallow water. The 1-layer model does not always give a propagating wave solution. If the radial frequency of the wave is larger than the limiting frequency ($\omega_{lim} = 2\sqrt{g/d}$) (SWASH, 2010), evanescent modes arise instead of propagating waves. Such a maximum does not exist in the 2-layer model. To demonstrate this behaviour, the Beji and Battjes (1993) experiment is modelled with both the 1-layer and 2-layer model. Two experiments with a different peak period, representing relatively shallower and deeper water, were modelled (See Table 7). The model is forced with the short wave measured timeseries at the first wave gauge. The long waves were computed based on the theory of Hasselmann (1962), because in contrast to the short waves, the measured long waves could contain reflective components. The grid resolution is set to 0.01 m, which corresponds to 20 grid cells for waves at 3 f_p. The same settings as the other validation cases were applied.

Before and on top of the bar both model versions agree well with the observations (Fig. 12 A, B, D and E) as the higher harmonics are bound to the primary wave components. When the bound waves are released as

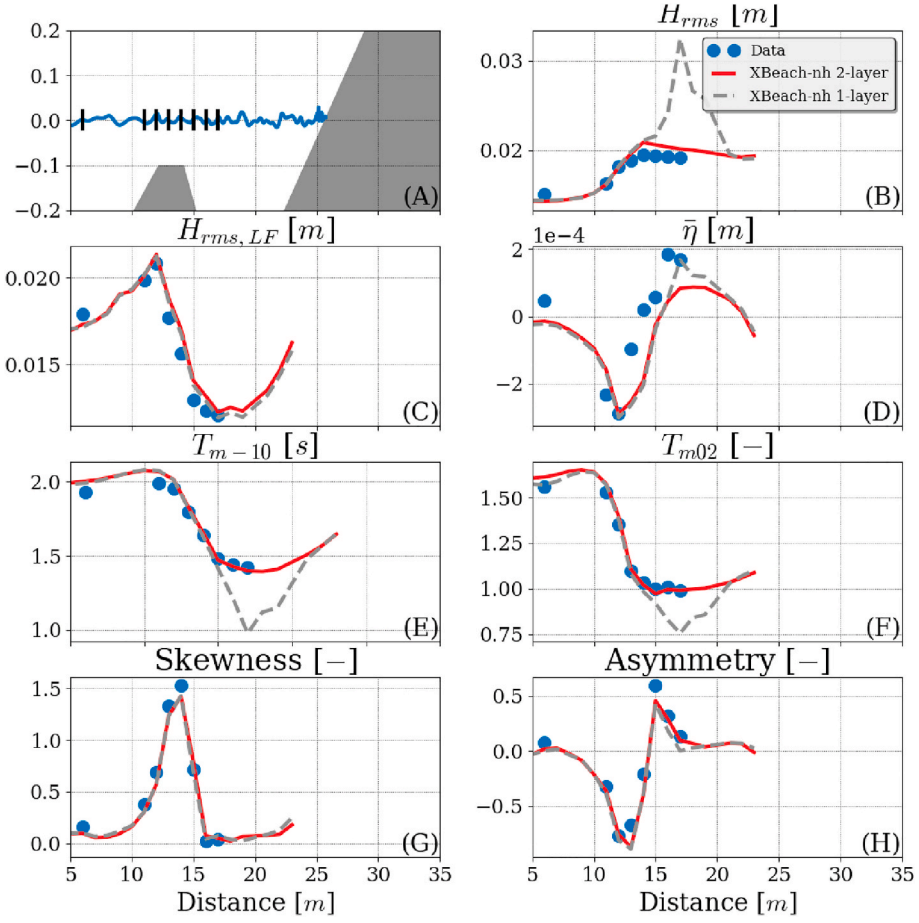

Fig. 11. The results of the validation with the Beji and Battjes (1993) observations. The red line is the result computed with the 2-layer model, the grey line those obtained with the 1-layer model, and the observations are shown with blue dots. The comparison is made for the total wave height (panel B), the LF-wave height (panel C), the setup (panel D), the spectral wave period (panel E), zero-crossing period (panel F), the skewness (panel G) and the asymmetry (panel H). In panel A the bed level and the instantaneous surface elevation is shown. (For interpretation of the references to colour in this figure legend, the reader is referred to the Web version of this article.)

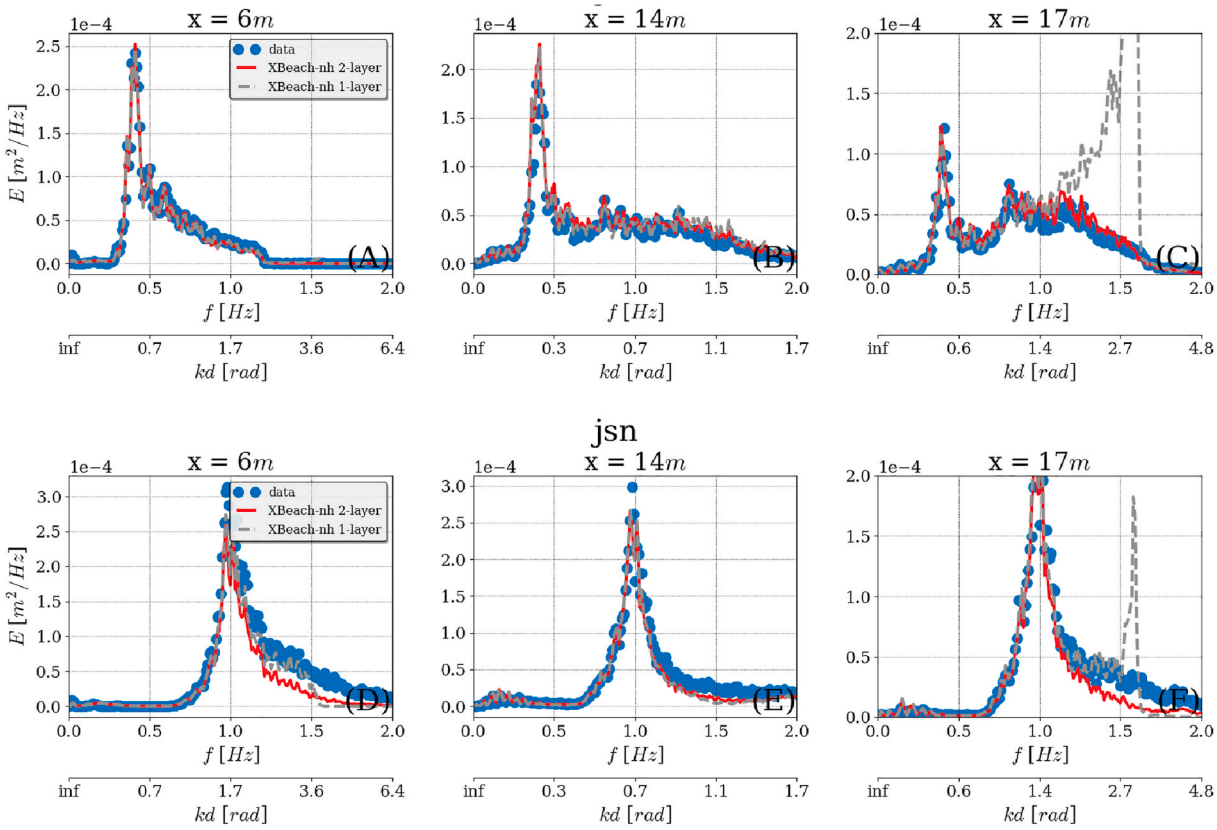

Fig. 12. Energy density spectrum for the Beji and Battjes (1993) experiment. The upper panel shows the results for experiment jln and the lower panel the results for experiment jsn. The blue dots shown the measured spectrums. The red and dashed grey line show the corresponding 2-layer and 1 -layer results. On the x-axis the frequency is shown with the first axis. The second axis shows the relative depth of this frequency component. (For interpretation of the references to colour in this figure legend, the reader is referred to the Web version of this article.)

free waves on the downslope, evanescent modes appear in the 1-layer model results, because part of the tail is above the limiting frequency which is given by 1.57 Hz at $x = 17$ m (See Fig. 12 panel C and F). The overestimation of the spectral shape results in incorrect predictions by the 1-layer model of the wave height and spectral periods (Fig. 11 B, E, F). Note that due to the relatively deeper water for test jsn, the energy of the bound waves is smaller and, therefore, the error of the free waves is smaller compared to test jln.

The 2-layer model does not show this unwanted behaviour and is in much better agreement with the observations. Moreover, the tail of the spectrum is much better captured (Fig. 12 C and F) and consequently the integral wave height and spectral period parameters are in much better agreement (Fig. 11 B, E and F). The other wave parameters do not show a large difference between both models, which indicate that the other hydrodynamic processes are accurately computed for both models.

It has been shown that the 2-layer model gives a better result for dispersion relation in deeper water by solving an additional equation. Due to the assumption of a constant non-hydrostatic pressure in the lower layer there is not much computational time compared to the 1-layer model. On average there is a 2%increase of computational time for both the Boers and Buckley experiment. Most of the computational time is needed to solve the non-hydrostatic pressure and, therefore, the computational time is not significantly larger than the 1-layer model.

6. Conclusion

A 2-layer non-hydrostatic model with improved dispersion behaviour is presented. Due to the assumption of a constant non-hydrostatic pressure distribution in the lower layer, the dispersive behaviour is improved without much additional computational cost. The 2-layer model can be applied until a kh of 4, whereas the 1-layer model is applicable till a kh of 1 based on a comparison with linear wave theory.

Due to the improved dispersion behaviour, the shoaling of waves in relative deep water is better captured. The 1-layer gives a large underestimation of the wave height when waves shoal from a kh of 2 to shallow water, whereas the 2-layer model shows similar results as linear wave theory.

A simulation of a laboratory experiment of a bichromatic wave group over a plane beach, showed that the 2-layer model is capable in simulating the energy transfer between the wave components. Both the reflection and dissipation of the sub-harmonic were accurately simulated. Moreover, the shape of the sub-harmonic was also correctly predicted. To validate the model performance for irregular waves, two laboratory tests were used as validation. Both the hydrodynamics at a fringing reef and barred beach were accurately reproduced.

The bulk wave height and spectral properties showed good agreement with the experimental data. The low frequency wave height, the setup and in particular the second order statistics contain more scatter, but the general trend was captured with the model. As an extension, the effects of using a model with better dispersion characteristics was shown for the wave transformation of irregular waves over a bar.

Thus, based on these validation cases it can be concluded that the 2-layer model can be applied to accurately simulate the bulk wave statistics and the spectral properties and to a lesser extend the second order statistics. Furthermore, the model showed good results for the complex bathymetries in shallow to intermediate water. Moreover, the 2-layer model extends the applicability to nearshore intermediate and shallow water with a kh limit of 4 compared to the 1-layer model which is limited to only shallow water with a maximum kh of 1.

Author declaration

Menno P. de Ridder: Writing - Original Draft, Formal analysis, Investigation and Validation.

Pieter B. Smit: Writing - Review & Editing, Writing - Original Draft, Formal analysis, Investigation, Software and Conceptualization.

Ap van Dongeren: Writing - Review & Editing and Supervision.

Robert McCall: Supervision and Writing - Review & Editing.

Kees Nederhoff: Formal analysis, Validation and Writing - Review & Editing.

Ad J. H. M. Reniers: Supervision and Writing - Review & Editing.

Declaration of competing interest

The authors declare that they have no known competing financial interests or personal relationships that could have appeared to influence the work reported in this paper.

Acknowledgements

This work has been carried out under funding by Delateres Strategic Research in the "Quantifying Flood Hazards and Impacts" program (11203750).

Appendix A. Resonant mismatch

The energy transfer between two wave components is related to the resonant mismatch given by: $\omega(k_1) + \omega(k_2) - \omega(k_1 + k_2)$. Thus, an error in the dispersion relation will affect the energy transfer between wave components. The relative error of the resonant mismatch with the linear dispersion relation shows that the 2-layer gives accurate results till a kh around 5, whereas the 1-layer model shows the same behaviour around $kh \approx 2$ (see Figure A13). This error is based on the numerical dispersion relation given in equation (25). This result shows that the 2-layer model gives a better result for the tail of the spectrum when kh becomes larger than 2.

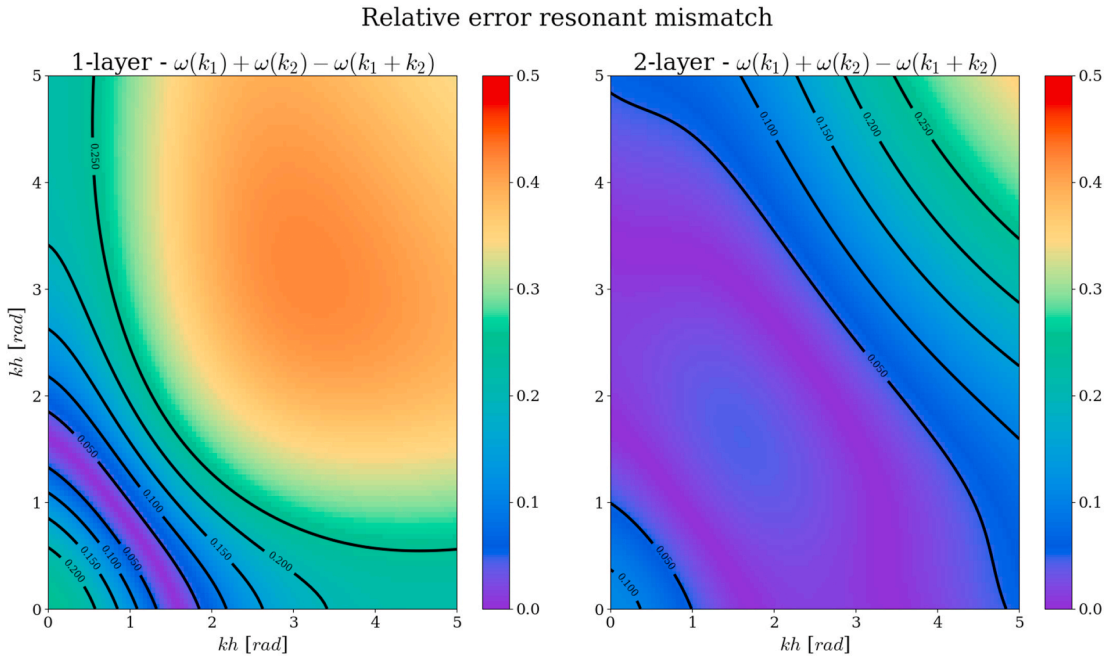

Fig. A.13. Relative error in the resonant mismatch with the linear dispersion relation for a interaction between two waves. The left panel shows the relative error for the 1-layer model and the right panel shows the relative error for the 2-layer model.

References

Agnon, Y., Sheremet, A., Gonsalves, J., Stiassnie, M., 1993. Nonlinear evolution of a unidirectional shoaling wave field. Coast. Eng. 20, 29–58.

Antuono, M., Brocchini, M., 2013. Beyond boussinesq-type equations: semi-integrated models for coastal dynamics. Phys. Fluids 25, 016603.

Bai, Y., Cheung, K.F., 2013. Depth-integrated free-surface flow with parameterized non-hydrostatic pressure. Int. J. Numer. Methods Fluid. 71, 403–421.

Battjes, J., Bakkenes, H., Janssen, T., Van Dongeren, A., 2004. Shoaling of subharmonic gravity waves. J. Geophys. Res.: Oceans 109.

Beji, S., Battjes, J., 1993. Experimental investigation of wave propagation over a bar. Coast. Eng. 19, 151–162.

Boers, M., 1997. Simulation of a surf zone with a barred beach; part 1: wave heights and wave breaking. Oceanogr. Lit. Rev. 4, 292.

Boers, M., 2005. Surf Zone Turbulence. Ph.D. thesis. Delft University of Technology.

Booij, N., Holthuijsen, L., Ris, R., 1996. The" swan" wave model for shallow water. Coastal Engineering Proceedings 1.

Brocchini, M., 2013. A reasoned overview on boussinesq-type models: the interplay between physics, mathematics and numerics. Proc. Math. Phys. Eng. Sci. 469, 20130496.

Buckley, M.L., Lowe, R.J., Hansen, J.E., Van Dongeren, A.R., 2015. Dynamics of wave setup over a steeply sloping fringing reef. J. Phys. Oceanogr. 45, 3005–3023.

Casulli, V., Stelling, G.S., 1998. Numerical simulation of 3d quasi-hydrostatic, free-surface flows. J. Hydraul. Eng. 124, 678–686.

Cavaleri, L., Alves, J.-H., Ardhuin, F., Babanin, A., Banner, M., Belibassakis, K., Benoit, M., Donelan, M., Groeneweg, J., Herbers, T., et al., 2007. Wave modelling–the state of the art. Prog. Oceanogr. 75, 603–674.

Cui, H., Pietrzak, J., Stelling, G., 2014. Optimal dispersion with minimized Poisson equations for non-hydrostatic free surface flows. Ocean Model. 81, 1–12.

Eldeberky, Y., 1997. Nonlinear transformation of wave spectra in the nearshore zone. Oceanogr. Lit. Rev. 4, 297.

Elgar, S., Guza, R., 1985. Observations of bispectra of shoaling surface gravity waves. J. Fluid Mech. 161, 425–448.

Ferreira, Ó., Ciavola, P., Armaroli, C., Balouin, Y., Benavente, J., Río, L.D., Deserti, M., Esteves, L., Furmanczyk, K., Haerens, P., et al., 2009. Coastal storm risk assessment in europe: examples from 9 study sites. J. Coast Res. 1632–1636.

Fiedler, J.W., Smit, P.B., Brodie, K.L., McNinch, J., Guza, R., 2019. The offshore boundary condition in surf zone modeling. Coast. Eng. 143, 12–20.

Hasselmann, K., 1962. On the non-linear energy transfer in a gravity-wave spectrum part 1. general theory. J. Fluid Mech. 12, 481–500.

Herbers, T., Burton, M., 1997. Nonlinear shoaling of directionally spread waves on a beach. J. Geophys. Res.: Oceans 102, 21101–21114.
Herbers, T., Elgar, S., Guza, R., 1995. Generation and propagation of infragravity waves. J. Geophys. Res.: Oceans 100, 24863–24872.
Jacobsen, N.G., Fredsoe, J., 2014. Formation and development of a breaker bar under regular waves. part 2: sediment transport and morphology. Coast. Eng. 88, 55–68.
Janssen, T.T., Herbers, T., 2009. Nonlinear wave statistics in a focal zone. J. Phys. Oceanogr. 39, 1948–1964.
Kirby, J.T., 2017. Recent advances in nearshore wave, circulation, and sediment transport modeling. J. Mar. Res. 75, 263–300.
Kirby, J.T., Wei, G., Chen, Q., Kennedy, A.B., Dalrymple, R.A., 1998. Funwave 1.0: Fully Nonlinear Boussinesq Wave Model-Documentation and User's Manual. Research Report NO. CACR-98-06.
Longuet-Higgins, M.S., Stewart, R., 1962. Radiation stress and mass transport in gravity waves, with application to 'surf beats'. J. Fluid Mech. 13, 481–504.
Ma, G., Shi, F., Kirby, J.T., 2012. Shock-capturing non-hydrostatic model for fully dispersive surface wave processes. Ocean Model. 43, 22–35.
Madsen, P., Sørensen, O., 1993. Bound waves and triad interactions in shallow water. Ocean. Eng. 20, 359–388.
Madsen, P.A., Sørensen, O., Schäffer, H., 1997. Surf zone dynamics simulated by a Boussinesq type model. Part I. Model description and cross-shore motion of regular waves. Coast. Eng. 32, 255–287, 10.1016/S0378-3839(97)00028-8. http://linkinghub.elsevier.com/retrieve/pii/S0378383997000288.
McCall, R.T., 2015. Process-based Modelling of Storm Impacts on Gravel Coasts. Ph.D. thesis. plymouth university. URL. https://pearl.plymouth.ac.uk//handle/10026.1/3929.
McCall, R.T., Van Thiel de Vries, J.S., Plant, N.G., Van Dongeren, A.R., Roelvink, J.A., Thompson, D.M., Reniers, A.J., 2010. Two-dimensional time dependent hurricane overwash and erosion modeling at Santa Rosa Island. Coast. Eng. 57, 668–683. https://doi.org/10.1016/j.coastaleng.2010.02.006.
McCall, R., Masselink, G., Poate, T., Roelvink, J., Almeida, L., Davidson, M., Russell, P., 2014. Modelling storm hydrodynamics on gravel beaches with xbeach-g. Coast. Eng. 91, 231–250.
McComb, P.J., Johnson, D.L., Beamsley, B.J., et al., 2009. Numerical study of options to reduce swell and long wave penetration at port geraldton. Coasts and Ports 2009: In a Dynamic Environment 490.
Pearson, S.G., Storlazzi, C.D., van Dongeren, A.R., Tissier, M.F., Reniers, A.J., 2017. A bayesian-based system to assess wave-driven flooding Hazards on coral reef-lined coasts. J. Geophys. Res.: Oceans 99–117. https://doi.org/10.1002/2017JC013204.
Quataert, E., Storlazzi, C., Van Rooijen, A., Cheriton, O., Van Dongeren, A., 2015. The influence of coral reefs and climate change on wave-driven flooding of tropical coastlines. Geophys. Res. Lett. 42, 6407–6415. https://doi.org/10.1002/2015GL064861.
Reniers, A.J., Roelvink, J., Thornton, E., 2004. Morphodynamic modeling of an embayed beach under wave group forcing. J. Geophys. Res.: Oceans 109.
Rijnsdorp, D.P., Smit, P.B., Zijlema, M., 2014. Non-hydrostatic modelling of infragravity waves under laboratory conditions. Coast. Eng. 85, 30–42.
Rijnsdorp, D.P., Smit, P.B., Zijlema, M., Reniers, A.J., 2017. Efficient non-hydrostatic modelling of 3d wave-induced currents using a subgrid approach. Ocean Model. 116, 118–133.
Roelvink, J., Reniers, A., Dongeren, A.V., Thiel, J.V., Vries, D., McCall, R., Lescinski, J., 2009. Modelling storm impacts on beaches , dunes and barrier islands. Coast. Eng. 56, 1133–1152. https://doi.org/10.1016/j.coastaleng.2009.08.006, 10.1016/j.coastaleng.2009.08.006.
Roelvink, J., McCall, R., Mehvar, S., Nederhoff, C., Dastgheib, A., 2017. Improving predictions of swash dynamics in XBeach: the role of groupiness and incident-band runup. Coast. Eng. 1–21. https://doi.org/10.1016/j.coastaleng.2017.07.004, 10.1016/j.coastaleng.2017.07.004.
Roelvink, D., McCall, R., Mehvar, S., Nederhoff, K., Dastgheib, A., 2018. Improving predictions of swash dynamics in xbeach: the role of groupiness and incident-band runup. Coast. Eng. 134, 103–123.
Salmon, J., Smit, P., Janssen, T., Holthuijsen, L., 2016. A consistent collinear triad approximation for operational wave models. Ocean Model. 104, 203–212.
Smit, P., Stelling, G., Roelvink, D., van Thiel de Vries, J., McCall, R., van Dongeren, A., Zwinkels, C., Jacobs, R., 2010. Xbeach: Non-hydrostatic Model. Report, Delft University of Technology and Deltares, Delft, The Netherlands.
Smit, P., Zijlema, M., Stelling, G., 2013. Depth-induced wave breaking in a non-hydrostatic, near-shore wave model. Coast. Eng. 76, 1–16. https://doi.org/10.1016/j.coastaleng.2013.01.008, 10.1016/j.coastaleng.2013.01.008.
Smit, P., Janssen, T., Holthuijsen, L., Smith, J., 2014. Non-hydrostatic modeling of surf zone wave dynamics. Coast. Eng. 83, 36–48.
Sorensen, O.R., Schäffer, H.A., Madsen, P.A., 1998. Surf zone dynamics simulated by a Boussinesq type model. III. Wave-induced horizontal nearshore circulations. Coast. Eng. 33, 155–176. https://doi.org/10.1016/S0378-3839(98)00007-6.
Stelling, G.S., Duinmeijer, S.A., 2003. A staggered conservative scheme for every froude number in rapidly varied shallow water flows. Int. J. Numer. Methods Fluid. 43, 1329–1354.
Stelling, G., Zijlema, M., 2003. An accurate and efficient finite-difference algorithm for non-hydrostatic free-surface flow with application to wave propagation. Int. J. Numer. Methods Fluid. 43, 1–23.
SWASH User Manual.2010 Delft University of Technology.
Symonds, G., Huntley, D.A., Bowen, A.J., 1982. Two-dimensional surf beat: long wave generation by a time-varying breakpoint. J. Geophys. Res.: Oceans 87, 492–498.
Thomas, T.J., Dwarakish, G., 2015. Numerical wave modelling–a review. Aquatic procedia 4, 443–448.
Van Dongeren, A., Reniers, A., Battjes, J., Svendsen, I., 2003. Numerical modeling of infragravity wave response during delilah. J. Geophys. Res.: Oceans 108.
Van Dongeren, A., Battjes, J., Janssen, T., Van Noorloos, J., Steenhauer, K., Steenbergen, G., Reniers, A., 2007. Shoaling and shoreline dissipation of low-frequency waves. J. Geophys. Res.: Oceans 112.
Van Rooijen, A., McCall, R., Van Thiel de Vries, J., Van Dongeren, A., Reniers, A., Roelvink, J., 2016. Modeling the effect of wave-vegetation interaction on wave setup. J. Geophys. Res.: Oceans 121, 4341–4359.
Zijlema, M., Stelling, G., Smit, P., 2011. Swash: an operational public domain code for simulating wave fields and rapidly varied flows in coastal waters. Coast. Eng. 58, 992–1012. https://doi.org/10.1016/j.coastaleng.2011.05.015, 10.1016/j.coastaleng.2011.05.015.